NAVAL POSTGRADUATE SCHOOL

MONTEREY, CALIFORNIA

THESIS

ENGINEERING OF NANOSCALE ANTIFOULING AND HYDROPHOBIC SURFACES ON NAVAL STRUCTURAL STEEL HY-80 BY ANODIZING

by

Thomas Samaras

June 2015

Thesis Advisor: Sarath K. Menon
Co-Advisor: Claudia C. Luhrs

THIS PAGE INTENTIONALLY LEFT BLANK

REPORT DOCUMENTATION PAGE

Form Approved OMB No. 0704–0188

1. AGENCY USE ONLY *(Leave blank)*	**2. REPORT DATE** June 2015	**3. REPORT TYPE AND DATES COVERED** Master's Thesis

4. TITLE AND SUBTITLE
ENGINEERING OF NANOSCALE ANTIFOULING AND HYDROPHOBIC SURFACES ON NAVAL STRUCTURAL STEEL HY-80 BY ANODIZING

5. FUNDING NUMBERS

6. AUTHOR(S) Thomas Samaras

7. PERFORMING ORGANIZATION NAME(S) AND ADDRESS(ES)
Naval Postgraduate School
Monterey, CA 93943-5000

8. PERFORMING ORGANIZATION REPORT NUMBER

9. SPONSORING /MONITORING AGENCY NAME(S) AND ADDRESS(ES)
N/A

10. SPONSORING/MONITORING AGENCY REPORT NUMBER

11. SUPPLEMENTARY NOTES The views expressed in this thesis are those of the author and do not reflect the official policy or position of the Department of Defense or the U.S. Government. IRB Protocol number ____N/A____.

12a. DISTRIBUTION / AVAILABILITY STATEMENT
Approved for public release; distribution is unlimited

12b. DISTRIBUTION CODE

13. ABSTRACT (maximum 200 words)

The impact that biofouling has on a ship's performance has long been recognized, since it increases the frictional resistance of the hull and can increase the ship's fuel consumption.

In this study, the spectrum of hydrophobic and antifouling surface patterns that can electrochemically be fabricated on HY-80 steel (alloy that is broadly used in shipbuilding for welded hull plates) is examined. After the fabrication of nanoscaled topographies, the optimum conditions for anodizing are determined by correlating the processing conditions with microstructural data. Characterization of the surface oxides was conducted by techniques such as Scanning Electron and Focused Ion Beam microscopy as well as identification of the formed phases by X-ray diffraction techniques.

Hydrophobicity of the surfaces was examined by measuring the contact angle of deionized water on the HY-80 steel surface. These studies revealed the improved wetting behavior of the anodized surfaces. Thermogravimetric analysis along with quantitative examination of the biofouling on the specimens were studied after prolonged exposure to seawater and indicated a decrease in the corrosion rate of anodized surfaces.

14. SUBJECT TERMS
steel, HY-80, anodization, biofouling, hydrophobic, anticorrosion, nanoporous

15. NUMBER OF PAGES
113

16. PRICE CODE

17. SECURITY CLASSIFICATION OF REPORT	**18. SECURITY CLASSIFICATION OF THIS PAGE**	**19. SECURITY CLASSIFICATION OF ABSTRACT**	**20. LIMITATION OF ABSTRACT**
Unclassified	Unclassified	Unclassified	UU

NSN 7540–01-280-5500

Standard Form 298 (Rev. 2–89)
Prescribed by ANSI Std. 239–18

THIS PAGE INTENTIONALLY LEFT BLANK

Approved for public release; distribution is unlimited

ENGINEERING OF NANOSCALE ANTIFOULING AND HYDROPHOBIC SURFACES ON NAVAL STRUCTURAL STEEL HY-80 BY ANODIZING

Thomas Samaras
Lieutenant, Hellenic Navy
B.S., Hellenic Naval Academy, 2004

Submitted in partial fulfillment of the
requirements for the degree of

MASTER OF SCIENCE IN MECHANICAL ENGINEERING

from the

NAVAL POSTGRADUATE SCHOOL
June 2015

Author: Thomas Samaras

Approved by: Sarath K. Menon
Thesis Advisor

Claudia C. Luhrs
Co-Advisor

Garth V. Hobson
Chair, Department of Mechanical and Aerospace Engineering

THIS PAGE INTENTIONALLY LEFT BLANK

ABSTRACT

The impact that biofouling has on a ship's performance has long been recognized, since it increases the frictional resistance of the hull and can increase the ship's fuel consumption.

In this study, the spectrum of hydrophobic and antifouling surface patterns that can electrochemically be fabricated on HY-80 steel (alloy that is broadly used in shipbuilding for welded hull plates) is examined. After the fabrication of nanoscaled topographies, the optimum conditions for anodizing are determined by correlating the processing conditions with microstructural data. Characterization of the surface oxides was conducted by techniques such as Scanning Electron and Focused Ion Beam microscopy as well as identification of the formed phases by X-ray diffraction techniques.

Hydrophobicity of the surfaces was examined by measuring the contact angle of deionized water on the HY-80 steel surface. These studies revealed the improved wetting behavior of the anodized surfaces. Thermogravimetric analysis along with quantitative examination of the biofouling on the specimens were studied after prolonged exposure to seawater and indicated a decrease in the corrosion rate of anodized surfaces.

THIS PAGE INTENTIONALLY LEFT BLANK

TABLE OF CONTENTS

LIST OF FIGURES

LIST OF TABLES

THIS PAGE INTENTIONALLY LEFT BLANK

LIST OF ACRONYMS AND ABBREVIATIONS

A	Ampere
Al	Aluminum
At%	Atomic Number Percent
BSE	Backscattered Electrons
C	Carbon
Cr	Chromium
cm	Centimeters
Cu	Copper
DI	Deionized Water
DSC	Differential Scanning Calorimeter
e^-	Electron
EG	Ethylene Glycol
EDS	Energy-dispersive X-ray Spectroscopy
EPS	Extracellular Polymeric Substances
Fe	Iron
FIB	Focused Ion Beam
h	Hour
H	Hydrogen
H_2SO_4	Sulfuric Acid
$HClO_4$	Perchloric Acid
HF	Hydrofluoric Acid
ICDD	International Centre for Diffraction Data
KOH	Potassium Hydroxide
KV	Kilovolts
LMIS	Liquid Metal Ion Source
m	Meter
mg	Milligram
Mg	Magnesium

min	Minute
ml	Milliliter
mm	Millimeter
Mn	Manganese
Mo	Molybdemun
MPY	Mils Penetration per Year
nA	Nano Amperes
NaCl	Sodium Chloride
NaOH	Sodium Hydroxide
NH_4F	Ammonium Fluoride
Ni	Nickel
nm	Nanometers
NPS	Naval Postgraduate School
P	Phosphorous
pA	Pico Amperes
QMS	Quadruple Mass Spectrometer
S	Sulfur
SE	Secondary Electrons
sec	Second
SEM	Scanning Electron Microscopy/Microscope
Si	Silicon
SiC	Silicon Carbide
Ta	Tantalum
TGA	Thermogravimetric Analysis
TBT	Tributyltin
TBTO	Tributyltin Oxide
Ti	Titanium
rpm	Revolutions per Minute
V	Volts
wt%	Weight Percent

w/v	Weight over Volume
XRD	X-ray Diffractometry/Diffractometer
Zr	Zirconium
µl	Microliter
µm	Micrometer

THIS PAGE INTENTIONALLY LEFT BLANK

ACKNOWLEDGMENTS

I dedicate this work to my wife, Betty, for her continuous loving support and patience, and to my newborn son for the happiness that he brought to my life.

This thesis would not have been possible without the invaluable support and wise guidance of my thesis advisor Professor Sarath Menon and co-advisor Claudia Luhrs. Both their professionalism and their wealth of knowledge shined like a beacon leading the way. Sincerely, I couldn’t have asked for more compassionate individuals as supervisors and I consider myself enlightened after having been their student.

I would also like to deeply thank all my friends and classmates for listening to me droning on about my thesis and for being there when I needed them the most. Wei Zhong and Nazmi, I wish you both the best of luck on your future endeavors.

Lastly and most importantly, I would like to thank the Hellenic Navy for believing in me and providing me with the opportunity to make a lifetime dream come true and study at one of the most prominent universities.

THIS PAGE INTENTIONALLY LEFT BLANK

I. INTRODUCTION

A. MOTIVATION

One of the major concerns in naval engineering has been the marine biofouling caused by the adhesion of living organisms in submerged seawater surfaces, whether on ship hulls, pipelines, or even marine structures such as platforms or bridge pillars. The negative effects that biofouling has on a ship's hull include the following: (i) bio corrosion that increases the chances of crevice corrosion, which can be devastating to the structure by resulting in premature structural failure, (ii) extensive maintenance, and (iii) increase of the surface roughness which in turn causes an increase in hydrodynamic drag and, therefore, an increase in the frictional resistance of the ship. Frictional resistance can account for as much as 90% of the ship's total drag [1] and, subsequently, this results in an approximately 40% increase to the ship's fuel consumption [2] or even the reduction of a ship's maximum speed up to 2 knots [3]. This has a tremendous economic impact, calculated in 2010 to be $2.3 million per ship in the U.S. Navy alone [1].

From ancient times, people have struggled with microbial attachment to vessels and since the origins of naval engineering, innovative methods have been used to overcome these problems. Ancient Phoenicians and Carthaginians used wax, tar, and asphalt, and there is even a record of arsenic and sulfur being used in 412 BC. These methods were used up until copper became the first successful antifouling surface to receive worldwide recognition [3].

Nowadays, the best established antifouling methods are "paints." Recent studies indicated that widely used organotin compounds such as tributyltin (TBT) and tributyltin oxide (TBTO) have been found to be toxic to marine organisms that are not related to biofouling [4], and subsequently their use has been forbidden from the Marine Environment Protection Committee of the International Maritime Organization [5]. Therefore, modern naval engineering is seeking new,

environmentally friendly ways of reducing biofouling. Novel approaches include increasing the ship surface's antifouling properties by increasing its hydrophobicity. A lot of research is being conducted in constructing micro or nano scale patterned surfaces that reduce wettability, and nano scale patterns were manufactured that can decrease biological fouling from 47% up to 86% [6, 7].

The development of biomimetic or bio-inspired materials has been suggested as a means to reduce barnacle attachment, and research in this area appears very promising. Studies on bio-inspired micro scale topographically rough surfaces for antifouling purposes have received a lot of interest, given the observation of reduced barnacle settlement on shark skin. The surface of the shark skin has grooves and fine scales (dermal denticles), and these features have inspired scientists to develop techniques based on lithographic patterning to reproduce similar artificial structures that are hydrophobic, which aid in the deterrence of bio-organism colonization as well [7, 8].

One of the techniques suggested by previous Naval Postgraduate School (NPS) studies to create hydrophobic/antifouling surfaces is anodization. This technique has been successful on aluminum [9], titanium [10] and their alloys indicating that this very simple and well-established method can provide extremely useful results in various applications such as energy storage materials, bio sensing, orthopedics [11, 12], and so forth. The hydrophobicity of anodized nanoporous structures has been reported, and the role of wettability in impeding biofouling, including barnacle attachment on surfaces, is well recognized [13]. Through a two-step high field anodization in phosphoric acid, J.C. Buijnsters et al[9]. produced 5 μm thick nanoporous anodized aluminum oxide films with average pore openings in the range of 140–190 nm, which reduced the wettability of aluminum alloy 1050 from approximately 92^{o} [14] up to 128^{o}. In the case of titanium, studies of P.V. Mahalakshmi et al. [10] indicated that precoating treatment by anodization in sulfuric acid (H_2SO_4) and hydrofluoric acid (HF) electrolyte bath for 1h at 30 V led to the development of super hydrophobic

titanium surfaces with contact angles of $148^0 \pm 4^0$ and increased microbial attachment resistance.

Metal anodizing techniques have been widely used to modify surfaces. Moreover, because the process increases corrosion and wear resistance and can also be applied to large marine structures, the technique is more appealing for applications in the shipbuilding industry than the patterning techniques.

B. LITERATURE REVIEW ON ANODIZATION

In the last decades, there have been plenty of reports on self-ordering electrochemical processes to prepare highly ordered oxide nanostructures. The majority of these studies focus on metals such as Al, Ti, Zr, and Ta [10, 15–18]. However, the self-organized porous alumina arrays grown by anodization on either pure aluminum or aluminum alloys represent the most studied system [9, 19–21].

Although iron is a widely used metal, only a few attempts can be found to electrochemically fabricate ordered oxide nanostructures on the surface of Fe-based metals.

Burleigh et al. published two reports in 2007 [22] and 2009 [23], followed by a patent in 2011 [24], presenting a novel method of anodizing steel in 10 wt% to saturated solutions of potassium hydroxide (KOH) and sodium hydroxide (NaOH). They produced anodized films consisting mainly of magnetite (Fe_3O_4) in both solutions (KOH and NaOH) that provide improved corrosion protection to steel.

The majority of studies on steel and iron anodization, though, focus on an ethylene glycol (EG)–based electrolyte containing dissolved ammonium fluoride (NH_4F) in deionized water (DI). Keyu Xie et al. [25] published extensive research on fabricating iron oxide (hematite) nanotubes on Fe foils through electrochemical anodization at an applied voltage between 30–50 V, in an EG-based electrolyte composed of 0.25–0.50 wt% NH_4F and 1–3 wt% DI water at

elevated temperatures of up to 60 ^{o}C. A similar method is also suggested by Sergiu Albu et al. [26] but with different anodization conditions of temperature, concentration, and applied voltage.

In a paper by Y. Konno et al. [27], a galvanostatic anodization was introduced in an EG-based electrolyte containing 0.1M NH_4F and 0.5M DI water in 20 ^{o}C that resulted in the formation of self-organized nanoporous anodic films, but in this case the research had been in done in low carbon steels (instead of Fe foils).

In a different electrolytic environment that consisted of 3–10 wt% Perchloric acid ($HClO_4$) and EG, W. Zhan et al. [28] succeeded in creating a 13 nm to 26 nm thickness film of nanoporous arrays on stainless steel by anodization. The oxide structures produced under these conditions granted the material significant visible light photo catalytic activities along with corrosion resistance.

In the research on anodization of Fe-based metal surfaces [22–25, 27, 28], the focus has been on the examination of the morphologies of the nanoporous structures and the evaluation of the anodization parameters such as anodization potential, time, temperature, and electrolyte composition on the oxide layer.

C. OBJECTIVES

The overall aim of this study was to examine the potential of anodized surfaces on improving the biofouling resistance and corrosion properties of hull steel. With that in mind, in this preliminary study, the overarching objective was the fabrication and characterization of nano-topographic structures using anodization processes on naval steel HY-80. Further objectives are the evaluation of the wetting and antifouling properties that these surface patterns may present. If either wettability or antifouling can be achieved through this simple industrial method, the impact on naval structural engineering will be profound. However, it must be noted that the anodized steel with iron oxide

nanoporous structures is unlikely to provide sufficient metallic corrosion protection due to the non-adherence of the oxide films. Further modification of the chemistry of the surface will be necessary for a practical application of this idea. Nevertheless, the results of this preliminary study will form the backbone for the further development of structures with sufficient corrosion and prolonged antifouling protection sufficient to be of practical application in many marine structures, specifically those of interest to the Navy worldwide.

D. THESIS TASKS

The current thesis study is focused on the following procedures:

- The initial aim is the production of homogeneous nanoporous structures, based on the methods proposed by Burleigh et al. [22, 23], Xie et al. [25], Albu et al. [26], and Konno et al. [27] and described in the literature review section. Since most of these reports refer to either anodization of pure iron or generalized steel alloys, appropriate alterations in anodizing parameters are applied in order to reach the desired result.
- Characterization will be conducted with scanning electron microscopy (SEM), X-ray diffractometry (XRD), and serial sectioning microstructures by focused ion beam (FIB) microscopy to observe the cross section of anodized products, on selected samples. After making tests with various anodizing techniques and evaluating each sample, expectations are to distinguish the optimum design process and the limitation for each pattern.
- Wettability studies are performed by measuring water drop contact angles on the created surfaces, to evaluate its hydrophobic or hydrophilic behavior.
- Preliminary corrosion resistance assessment by weight loss measurements of anodized samples in stagnant Monterey seawater will provide information on their anti-corrosive properties. A limited amount of biofouling could be expected under these conditions and will be examined by optical and scanning electron microscopy studies.
- Finally, with the use of thermogravimetric analysis (TGA) and SEM quantitative analysis, an examination of the antifouling properties completes this study.

THIS PAGE INTENTIONALLY LEFT BLANK

II. BACKGROUND

A. BIOFOULING MECHANISMS

Biofouling (biological fouling) is defined as the accumulation of living organisms, such as macro algae, hydrozoans, bryozoans, barnacles, polychaete tubeworms, mollusks, and ascidians on artificial surfaces by adhesion, growth, and reproduction. Biofouling can be characterized into two main categories: micro fouling and macro fouling.

Micro fouling is the initial stage of biofouling and describes the formation of biofilm organisms, which are bacteria and diatoms on submerged structures. Biofilms are ubiquitous, as long as surfaces are exposed to seawater [2]. Minutes after a surface has been submerged in water, it absorbs a molecular film that consists of dissolved organic material. Within the next few hours, this film is colonized by bacteria, unicellular algae (especially diatoms), and/or cyanobacteria (blue-green algae), which together form a biofilm—an assemblage of attached cells, which is commonly referred to as *slime* [29].

These microorganisms adhere to the surface by extracellular polymeric substances (EPS). So the biofilm, which is the result of micro fouling, comprises both the microorganisms and the EPS, and thus the physical properties of the surface change, making it more amenable for the settlement of macro-fouling organisms. Then, the attached cells further divide, giving rise to colonies that eventually coalesce to form a compact biofilm, which in some cases may even achieve a thickness of 500 μm [29].

Macro fouling in the submerged surface occurs after two or three weeks, when micro-fouling organisms finally have evolved into a complex biological community and have chemically prepared the surface for the settlement of macro-fouling species. Macro-fouling organisms settle, develop, and overgrow the micro-fouling surface. The most important macro-fouling species are barnacles, algae, mussels, polychaete worms, bryozoans, and seaweed [2].

A macro-fouling community consists of either *soft fouling* or *hard fouling*. Soft fouling comprises algae and invertebrates, such as soft corals, sponges, anemones, tunicates, and hydroids, whilst hard fouling comprises invertebrates such as barnacles, mussels, and tubeworms.

The specific organisms that develop in a fouling community depend on the substratum, geographical location, season, and factors such as competition and predation [29]. Fouling is a highly dynamic process; an over-simplified schematic example of its evolution appears in Figure 1.

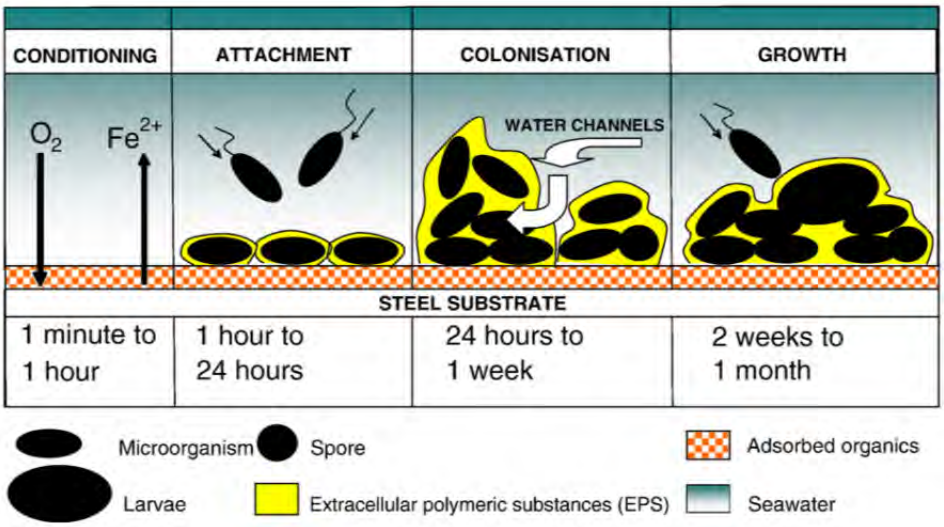

Figure 1. Schematic of biofouling stages on steel substrate, from [30]

B. APPLICATIONS AND PROPERTIES OF NAVAL STEEL HY-80

The HY (High Yield) series of steels have been used in U.S. naval warships since the 1950s. HY-80 steels (military specification MIL-S-16216) are broadly used in shipbuilding for welded hull plates and structural use, due to their excellent weldability and notch toughness, along with their good ductility even in welded sections.

The HY-80 steels are metallurgically classified as quenched and tempered martensitic steels. They have a martensitic microstructure resulting from the

combination of alloying, which can be seen in Table 1, and heat treatment employment to provide the optimal combination of strength and toughness.

This heat treatment consists of two procedures. The austenization in the ranges of 844 °C to 899 °C, followed by a water quench, and the tempering in the range of 621 °C to 677 °C (and in no case less than 600 °C), followed also by a water quench [31].

Following this heat treatment, the alloy develops a martensitic structure (the final product should contain more than 80% martensite), which provides to metal the desired mechanical properties of Table 2 and the physical properties of Table 3.

The alloying elements promote martensitic formation, but the alloying element with the major effect in producing a martensitic structure is carbon. The as-quenched steel manifests high strength and hardness but also is brittle and susceptible to hydrogen (cold) cracking [32].

Table 1. Chemical composition of HY-80 steel, after [33]

Element	(wt%)
Carbon (C)	0.10–0.20
Phosphorous (P)	0.020 max
Manganese (Mn)	0.010–0.46
Silicon (Si)	0.12–0.38
Sulfer (S)	0.020 max
Nickel (Ni)	1.93–3.32
Chromium (Cr)	0.94–1.86
Molybdenum (Mo)	0.17–0.63
Vanadium (V)	0.030 max
Titanium (Ti)	0.020 max
Copper (Cu)	0.25 max

Table 2. Mechanical properties of HY-80, after [32, 34]

Yield strength	552 Mpa
Elongation	20%
Reduction of area	50%
Charpy impact	81 J at -18 °C and 48 J at -84 °C
Transverse dynamic tear test	610 J at -40 °C

Table 3. Physical properties of HY-80, after [35]

Hardness (Rockwell)	C-21
Elastic Properties	
Elastic modulus, E	207 (GPa)
Poisson's Ratio, v	0.30
Shear modulus, E/2 (1+ v)	79 (GPa)
Bulk modulus, E/3 (1-2v)	172 (GPa)
Thermal Properties	
Density, ρ	7746 (kg/m^3)
Conductivity, k	34 (W/mK)
Specific heat, c_ρ	502 (J/kgK)
Diffusivity, k/ ρ c_ρ	$9x10^{-6}$ (m^2/s)
Expansion coef. (Vol), α	$11x10^{-6}$ (K^{-1})
Melting temperature, T_{MELT}	1793 (K)

C. PRINCIPLE OF ANODIZATION

Anodization, or anodic oxidation, is a well-established, low-cost industrial surface modification process that was discovered back in the early 1930s [12]; it is an electrochemical process developed not only to improve the native protective oxide films created on the surface of metals by making them more stable and highly resistant, but also to modify the surface by giving it a desired morphology. Ferrous alloys such as HY-80 have a very high chemical affinity for oxygen and rapidly corrode in aqueous media [36].

Iron can be oxidized to different valence states such as FeO, Fe_2O_3, and Fe_3O_4. The typical chemical reaction for anodizing iron in valence state 3 in an aqueous solution is illustrated below in equations (1) to (5), while an anodization setup of Fe is shown in Figure 2.

$$H_2O \rightarrow 2H^+ + O^{2-} \quad (1)$$

In the anode:

$$Fe \rightarrow Fe^{3+} + 3e^- \quad (2)$$

$$2Fe^{3+} + 3O^{2-} \rightarrow Fe_2O_3 \quad (3)$$

Overall process:

$$2Fe + 3H_2O \rightarrow Fe_2O_3 + 6H^+ + 6e^- \quad (4)$$

In cathode:

$$6H^+ + 6e^- \rightarrow 3H_2(gas) \quad (5)$$

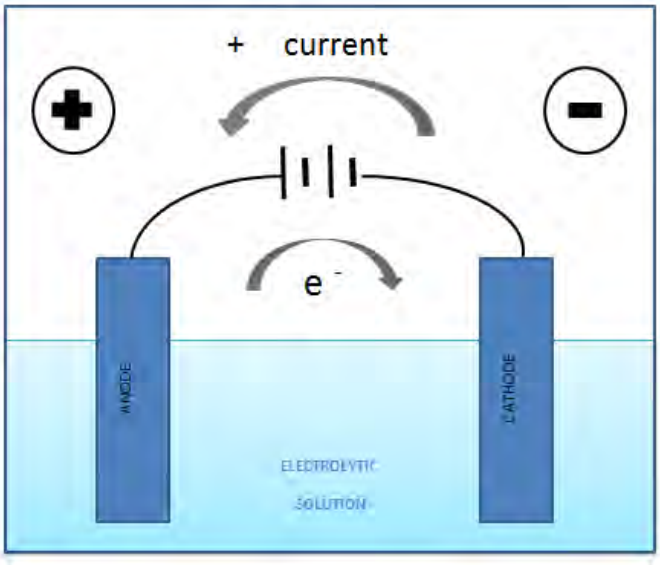

Figure 2. Schematic of a typical anodization setup

THIS PAGE INTENTIONALLY LEFT BLANK

III. MATERIALS AND CHARACTERIZATION METHODS

A. MATERIALS

1. Steel Samples

A plate of HY-80 steel was obtained from the Naval Surface Warfare Center (Carderock Division, Bethesda, MD). A small piece from this plate was sent for chemical analysis to Anamet, Inc. (Hayward, CA) to determine if the material procured was in fact HY-80 by composition. Additional elemental identification was performed using the energy-dispersive X-ray spectroscopy (EDS) technique to verify that the chemical composition of the samples matched the chemical composition specifications of HY-80, as previously described in Table 1. The results, as can be seen in the diagram of Figure 3 and in Tables 4 and 5, corroborate the quality of the samples.

Table 4. Elemental composition of steel sample analyzed at Anamet, Inc

Element	Min (wt%)	Max (wt%)
Carbon (C)	---	0.18
Chromium (Cr)	1.00	1.8
Copper (Cu)	---	0.25
Manganese (Mn)	0.10	0.40
Molybdenum (Mo)	0.20	0.60
Nickel (Ni)	2.00	3.25
Phosphorous (P)	---	0.025*
Silicon (Si)	0.15	0.35
Sulfer (S)	---	0.025*
Titanium (Ti)	---	0.02
Vanadium (V)	---	0.03

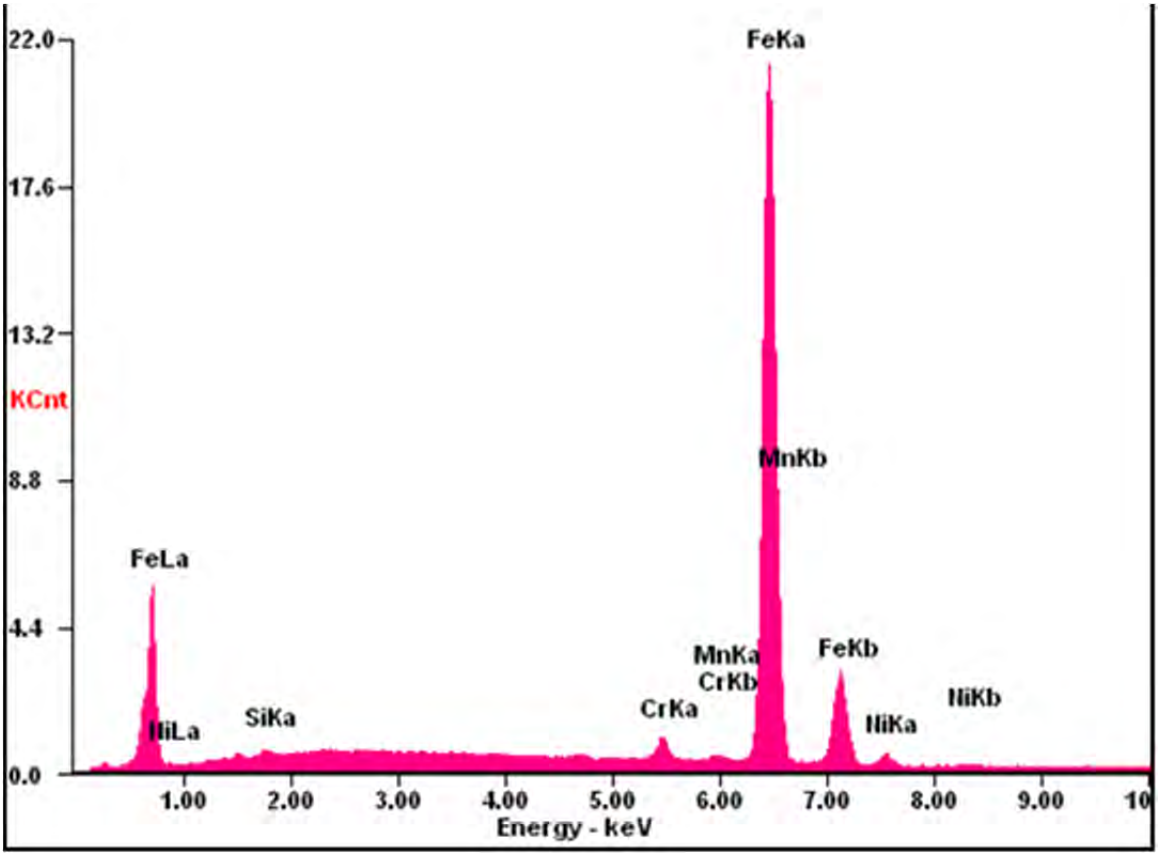

Figure 3. EDS spectrum from HY-80 steel

Table 5. EDS quantitative analysis showing weight and atomic number percent of elements in HY-80 steel

Element	**Wt%**	**At%**
Silicon (Si)	00.35	00.71
Chromium (Cr)	01.62	01.73
Manganese (Mn)	00.46	00.46
Iron (Fe)	95.54	95.17
Nickel (Ni)	02.03	01.92
Matrix	Correction	ZAF

Prior to any experimental procedure, the steel was cut to the desired dimensions, 17.5 mm × 5.7 mm × 0.8 mm, using the Struers Secotom-10 table-top precision cut-off machine (Figure 4) with a Struers Alumina cut-off wheel 50A20 (200 mm diameter × 0.8 mm × 22 mm diameter) at 2000 rpm and 30 mm/sec speed.

Figure 4. Struers Secotom-10 table-top precision cut-off machine

Grinding and polishing of specimens were conducted on a Buehler Ecomet 4 automatic polisher (Figure 5) at high speeds (100 rpm) starting with waterproof silicon carbide paper (SiC) 320 grit and gradually increasing to SiC 800 grit, SiC 1200 grit and SiC 2500 grit. Further polishing was conducted on a Buehler Ecomet 3 automatic polisher (Figure 5) with Buehler alumina/silica micro cloth grinding pad, 1 micron sized at moderate speeds. Polishing time for the most abrasive papers was typically 20 min, and up to 40 min for the finer grit.

Figure 5. Ecomet 4 (left) and Ecomet 3 (right) automatic polishers

2. Chemical Reagents

Sodium hydroxide (NaOH) was purchased from EMD Chemical Inc. (Gibbstown, NJ), and ammonium fluoride (NH_4F) and ethylene glycol (EG) 99.8% were purchased from Aldrich Chemistry (St. Louis, MO). All of the mentioned reagents were used as received, unless otherwise mentioned.

3. Lab Ware (Glassware and Metalware)

All lab ware (i.e., test tubes, vials, droppers, spatulas, etc.) was cleaned in a laboratory sink following a regime that involved a detergent wash and a minimum of three DI water rinses. The DI water was purchased from Weber Scientific. The detergent wash consisted of commercial dishwasher detergent in a solution of tap water. Following the cleaning procedure, all glass and metal ware were left to air dry overnight until use.

B. CHARACTERIZATION METHODS

1. Scanning Electron Microscopy (SEM)

Scanning Electron Microscopy (SEM) is the most widely used type of electron microscope [37]. In SEM, an electron gun produces a beam of monochromatic electrons. This beam passes through the condenser lens producing a coherent beam, which is focused onto the sample surface through an objective lens. The electron beam thus focused on the specimen is scanned across the specimen surface [38]. When an electronic beam strikes the specimen, due to various interactions, a variety of signals are generated, as shown in Figure 6. From this impact, electrons are emitted as a result of elastic and inelastic scattering, resulting in backscattered electrons (BSE) and secondary electrons (SE), respectively. SEM collects these electrons through detectors, amplifies them, and reconstructs a digital image of the surface of the specimen. Both signals give useful information in the imaging process with the SEs to be the primary signals for achieving topographic contrast, and the BSEs for the formation of elemental composition contrast.

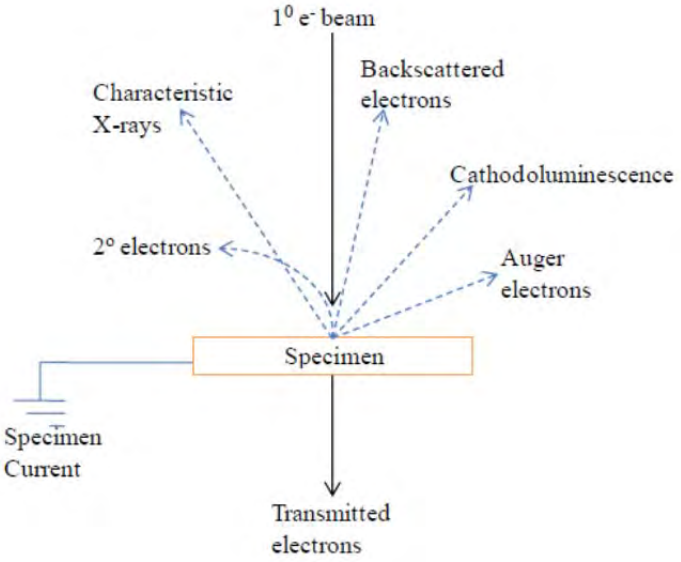

Figure 6. Specimen interaction with electron beam, from [38]

A Zeiss Neon 40 Crossbeam Scanning Electron Microscope with a Schottky type field emission electron source (Figure 7) was used to determine the topography, morphology, and size distribution of the constructed structures.

Figure 7. The Scanning Electron Microscopy setup

The system was energized to 2 KV and a beam current of 100pA was found to be ideal to image the anodized steel surface without the need for a

conducting metal coating. An exception to this procedure was the preparation of biofouled samples. To ensure electrical continuity, a requirement for SEM, each sample was prepared by applying a thin coating layer of Pt20Pd using the DC magnetron High Resolution Sputter Coater Cressington 208HR with rotary-planetary-tilt stage thickness controller MTM-20, as seen in Figure 8. Analysis was conducted using the SmartSEM V05.04.03.00 software package developed by Carl Zeiss SMT Ltd, and quantitative analysis, when needed, through ImageJ, a public domain Java image processing and analysis software.

The preparation of the samples for SEM analysis consisted of their drying in a stream of compressed air. They were kept in a -32 bar Pelco 2251 vacuum Desiccator (Figure 9) overnight, prior to being mounted on the chamber specimen holder.

Figure 8. DC magnetron High Resolution Sputter Coater

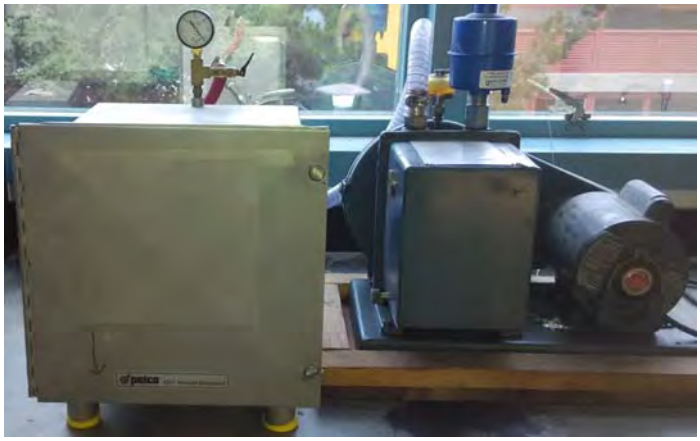

Figure 9. Vacuum chamber (on left) and dual-seal vacuum pump (on right) by Welch Manufacturing Co. (Chicago, IL)

2. Energy-Dispersive X-ray Spectroscopy (EDS)

Energy-dispersive X-ray spectroscopy (EDS) is a chemical microanalysis method that is used in conjunction with electron microscopy equipment. EDS is used to determine the presence and quantities of chemical elements of a specimen by detecting characteristic X-rays that are emitted from atoms irradiated by a high-energy electron beam. The emitted X-ray has an energy characteristic of the parent element, allowing for it to be specifically identified. The pattern obtained by this method contains peaks in various positions displaying the energy levels of each scattered X-ray corresponding to a certain element [38].

EDS measurements were carried out using an EDAX Pegasus system with an Apollo 10 Silicon Drift Detector.

The system was energized to 20 KV, 1nA current, 0° stage angle. Data were collected and analyzed using Genesis Spectrum software package developed by EDAX.

3. X-ray Diffractometry/Diffractometer (XRD)

X-ray diffractometry (XRD) is the most widely used X-ray diffraction technique in materials characterization. Inside the XRD, an X-ray beam of a

specific wavelength is used in order to analyze polycrystalline specimens and obtain their diffractogram (spectrum of diffraction intensity versus the angle between incident and diffraction beam) by constantly changing the incident angle of the beam. XRD is a useful technique to identify the crystallographic structure of a material, by correlating its obtained diffractogram with available databases, containing diffraction spectra of known crystalline substances [37].

X-ray diffractograms were obtained at room temperature using a Rigaku Miniflex 600 diffractometer equipped with a D/teX Ultra (Si high speed) 1D Detector (Figure 10) with a 600W x-ray generator, which was operated by Rigaku Miniflex Guidance Software, Version 1.4.0.2, with power settings of 40 kV and 15mA. Measurements were made by step scanning in the 2θ angle range 20°–90°, with a step size of 0.02° and a dwell time of 5 deg/min. Total run time per sample was 15 min.

The resulting intensity versus diffraction angle (2θ) was analyzed using the Rigaku PDXL2 software package, Version 2.2.2.0. Once measured, these diagrams were compared to those of the International Centre for Diffraction Data (ICDD)–compiled standards and the PDXL2 software to calculate the probability of sample match.

Figure 10. Rigaku Miniflex 600 X-ray Diffractometer

4. Focused Ion Beam (FIB)

The focused ion beam technique is a relatively new characterization method, commercially introduced in the 1980s [39]. The main components of the FIB system are normally a vacuum system, a liquid metal ion source (LMIS), an ion optics column, a sample stage with three axis translation, rotation and tilt capabilities, detectors, and a gas delivery system. All of these are remotely controlled through pre-installed software in an operating system. Due to the many similarities between this instrument and the scanning electron microscope, FIB rarely appears as a stand-alone single beam instrument, but most of the times is incorporated into SEM [40].

When an ion impinges on a solid, ion loses kinetic energy through interactions with the sample atoms. This transfer of energy from the ion to the solid results in a number of different processes:

- ion reflection and backscattering
- electron emission, which enables imaging
- electromagnetic radiation
- sputtering of neutral and ionized substrate atoms
- sample damage through atomic displacement
- sample heating though emission of photons [41, 42]

The basic functions of FIB are imaging, sputtering, and deposition; their main principles are illustrated in Figure 11. The function that has been exploited in this study is milling, a process which is a combination of physical sputtering and material deposition. The equipment used was a Zeiss Neon 40 Crossbeam Scanning Electron Microscope with a Schottky type field emission electron source and Canion 31 FIB column with a gallium liquid metal ion source.

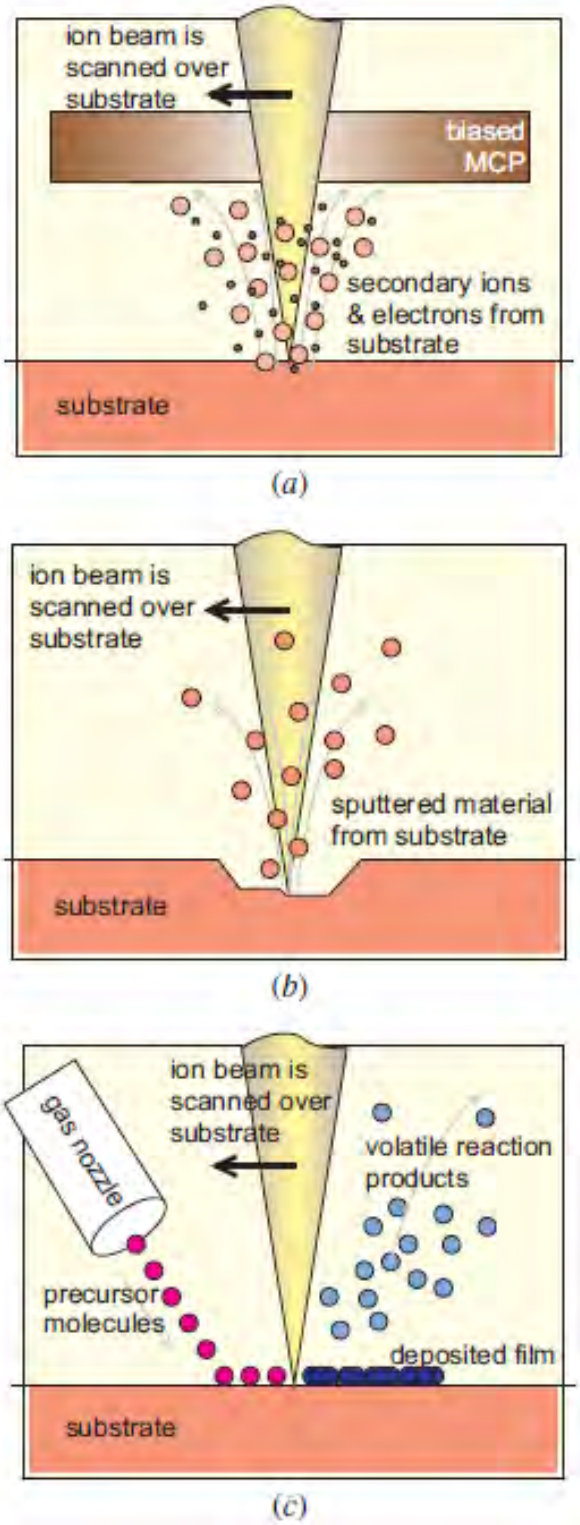

Figure 11. Principles of FIB: (a) imaging (b) sputtering–milling (c) deposition, from [41]

5. Differential Scanning Calorimeter (DSC) and Thermal Gravimetric Analysis (TGA)

Differential Scanning Calorimetry (DSC) and Thermal Gravimetric Analysis (TGA) are two thermal analysis techniques. They analyze changes in a property of a sample, which is related to an imposed temperature alteration.

DSC measures the heat flow of a sample and compares it with a reference. DSC devices measure the enthalpy changes of a sample during a thermal event, where the sample is heated under a constant heating rate. Then using pre-installed computer software, a DSC curve is plotted to illustrate the heat flow against changes in temperature [37].

TGA, on the other hand, measures mass changes of a sample with temperature. Following the same principles as the DSC, the sample is heated, either with a constant heating rate or at a constant temperature (in a controlled environment), and through a micro balance, changes in its mass are monitored. Then, by pre-installed computer software, a TGA curve is plotted that illustrates the mass change versus temperature. The main application of TGA is to analyze material decomposition as a function of temperature or as a function of time.

Both DSC and TGA were accomplished using a NETZSCH STA 449 F3 Jupiter simultaneous thermal analysis machine, as shown in Figures 12 and 14. Additionally, the evolved gases from the samples were analyzed by coupling the TGA/DSC with the NETZSCH TA-QMS 403C Aėolos quadruple mass spectrometer (QMS; Figures 13 and 14).

The thermal analyses were conducted in a constant heating rate of 10 °C/min from room temperature to 600 °C, under nitrogen atmosphere. Prior to TGA and DSC experiments with steel specimens, a run with an empty crucible was performed, under the same conditions, in order to obtain a correction curve. The correction curve was taken into consideration and experimental data were automatically calibrated using NETZCH Proteus Analysis Software.

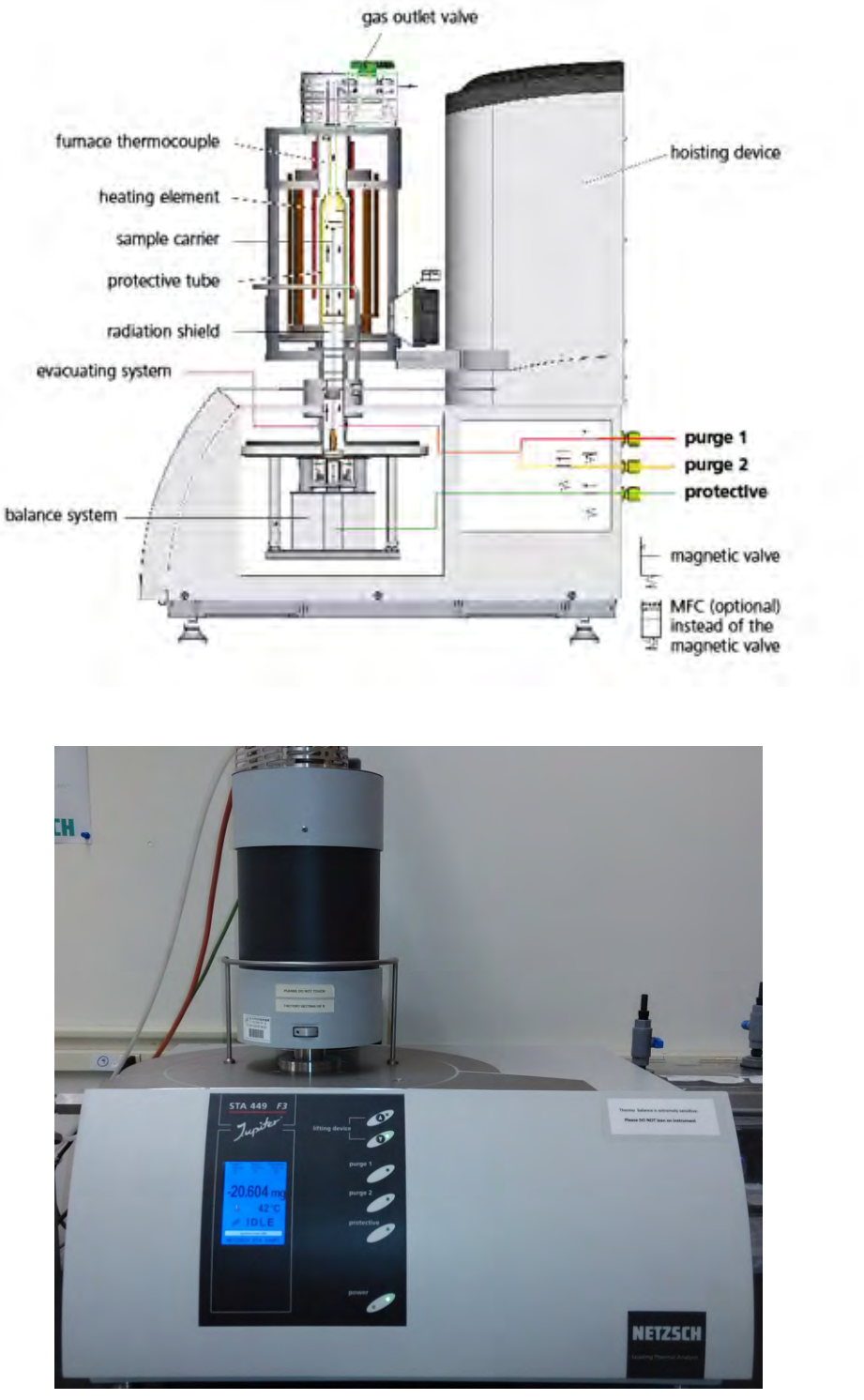

Figure 12. Diagram of NETZSCH STA 449 F3 Jupiter DSC/TGA (top) and picture of setup in NPS laboratory (bottom), from [43]

Figure 13. Diagram of NETZSCH TA-QMS 403C Aėolos QMS (left) and picture of setup in NPS laboratory (right), from [43]

Figure 14. TGA/DSC coupled with the quadruple mass spectrometer (QMS)

6. Contact Angle Measurement

The effect of the anodized steel surfaces with nanoporous oxides on hydrophobicity was determined by measuring contact angles. The experiments were performed at room temperature, with water droplets of ~ 34.3 µl volume; after letting the droplet stay one minute on the steel surface, photographs of the surface were captured with a Dino-Lite Pro AM413TA handheld digital optical Microscope (Figure 15) to record the droplet shape, and an ImageJ software package was used to analyze and measure the angle. To enhance the accuracy of the measurements, images of the same droplets were taken from various angles, and each experiment was repeated several times (6–38) until consistency was obtained.

Figure 15. Dino Lite optical microscope

The captured angles were analyzed in ImageJ software and the contact angle, $\theta_{c,}$ was measured, as illustrated in Figure 16.

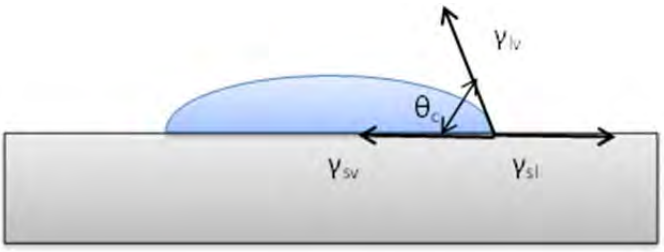

Figure 16. Contact angle measurement, where θ_c is the contact angle, and γ_{sl}, γ_{sv}, and γ_{lv} are the solid–liquid, solid–vapor and liquid–vapor interfaces, respectively

7. Corrosion Rate Measurement

The corrosion rate in the HY-80 steel samples was calculated from the measured weight loss, using a Dhaus Adventurer Pro precision balance (Figure 17) with a readability of 0.1 mg. The weight changes of the samples were determined after exposure in seawater (obtained from Monterey Bay) for a period of 10 days. Prior to water deposition, the un-anodized part of the specimen was cut off using a Buehler Isomet low speed saw with a Buehler 15 HC diamond wafering blade; electroplater's tape covered the non-anodized side of the specimen, leaving only the anodized side exposed. Upon removing from the corrosive environment, the samples were rinsed in DI water and dried in stream of compressed air to remove the non-adherent oxides. For reference reasons, experiments were also contacted in a 3.5 wt% NaCl aqueous solution.

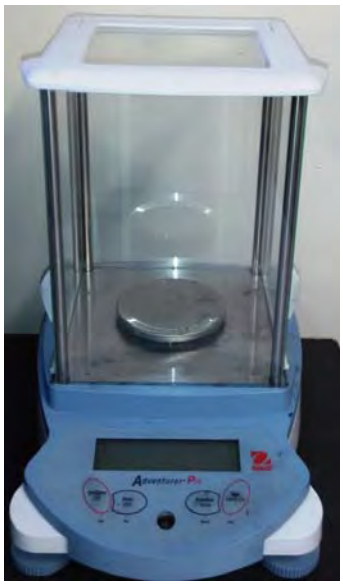

Figure 17. Dhaus Adventurer Pro micro balance

The corrosion rate was calculated in mils (1 mil = 0.001 in) penetration per year (MPY) and in mm/yr using the following equations:

$$MPY = \frac{534W}{DAT} \tag{6}$$

$$mm/yr = \frac{87.6W}{DAT} \tag{7}$$

where W is weight loss in milligrams, D is density in grams per cubic centimeter, T is time in hours, and A is area in square inches, in the case of MPY, and square centimeters, in the case of mm/yr. We chose the unit MPY since it is the most well-established corrosion rate unit in the United States [44] and the mm/yr unit (1 mm/yr = 39.37 MPY) in order to be consistent with the metric system.

IV. EXPERIMENTAL PROCEDURES

Based on previous studies on iron and iron-based metal anodization, which were described in the Literature Review on Anodization section, four different methods were selected in order to produce nano-topographic structures on HY-80 steel. The first method was initially proposed by Burleigh et al. [23] and involves anodization of steel in a 50 wt% NaOH aqueous solution, at elevated anodizing temperatures (between 30 °C to 90 °C) and under applied voltage of a range from 1.6 to 2.5 V. Nevertheless, after having carried out a few experiments in a variety of anodization parameters, the results of the created structures led to the selection of an alternative electrolyte.

In the next three anodization methods, experiments were contacted by using the most well established electrolyte for iron-based metal anodization, which is dissolved NH_4F in DI water into an EG solution. Two different potentiostatic techniques were examined as they were presented by Xie et al. [25] and Albu et al. [26], as well as a galvanostatic procedure presented by Konno et al. [27]. Both anodizing techniques established by Xie et al. [25] and Albu et al. [26] have reported the formation of nanoporous anodic oxides layer on Fe foils, but in the first case this occurred in an optimum condition of 50 V applied voltage, in an electrolyte of 0.50 wt% NH_4F and 3 wt% DI water, at 60 °C, while in the second case, it occurred at 40 V constant voltage in an electrolyte of 0.37 wt% NH_4F and 1.8 wt% DI water, at a temperature of 20 °C. However, the technique proposed by Konno et al. [27] was applied in low carbon steel (between 0.001 to 0.213 mass % carbon) under constant 50 A/m^{-2} current density, EG electrolyte containing 0.37 wt% NH_4F and 0.9 wt% DI water at a 20 °C anodizing temperature.

In each of the proposed methods in this study, the voltage, time, and anodizing temperature parameters widely varied from those of the original papers in pursuit of the optimum anodizing condition that will result in a self-oriented

nanoporous structure in the examined steel alloy (HY-80). Each method is explained in greater detail and is summarized in Table 6.

A. NAOH-BASED ELECTROLYTE

For this (as well as the following) anodizations, the experimental setup shown in Figure 19 was used.

Prior to anodization, the as-prepared steel samples (described in Chapter III) were further degreased by one-minute ultra-sonication steps in acetone, ethyl alcohol, and DI water, successively, in the 2510 Branson ultrasonic cleaner sonication bath shown in Figure 18. Finally, the samples were dried in a compressed air steam; electroplater's tape covered one side of the specimen, leaving only one side exposed to the electrolyte.

Figure 18. Picture of the ultrasonic cleaner

The to-be anodized steel panel was connected to the positive terminal (the anode) of the power supply parallel to a graphite panel of the same dimensions that was connected to the negative terminal (the cathode). The spacing between the anode and cathode was 2.5 cm with the non-tape covered side of the steel sample facing the graphite cathode. The potentials were applied using three

Power Designs Ambitrol 4005 Transistorized Power Supplies–40V-500 mA, in series connection.

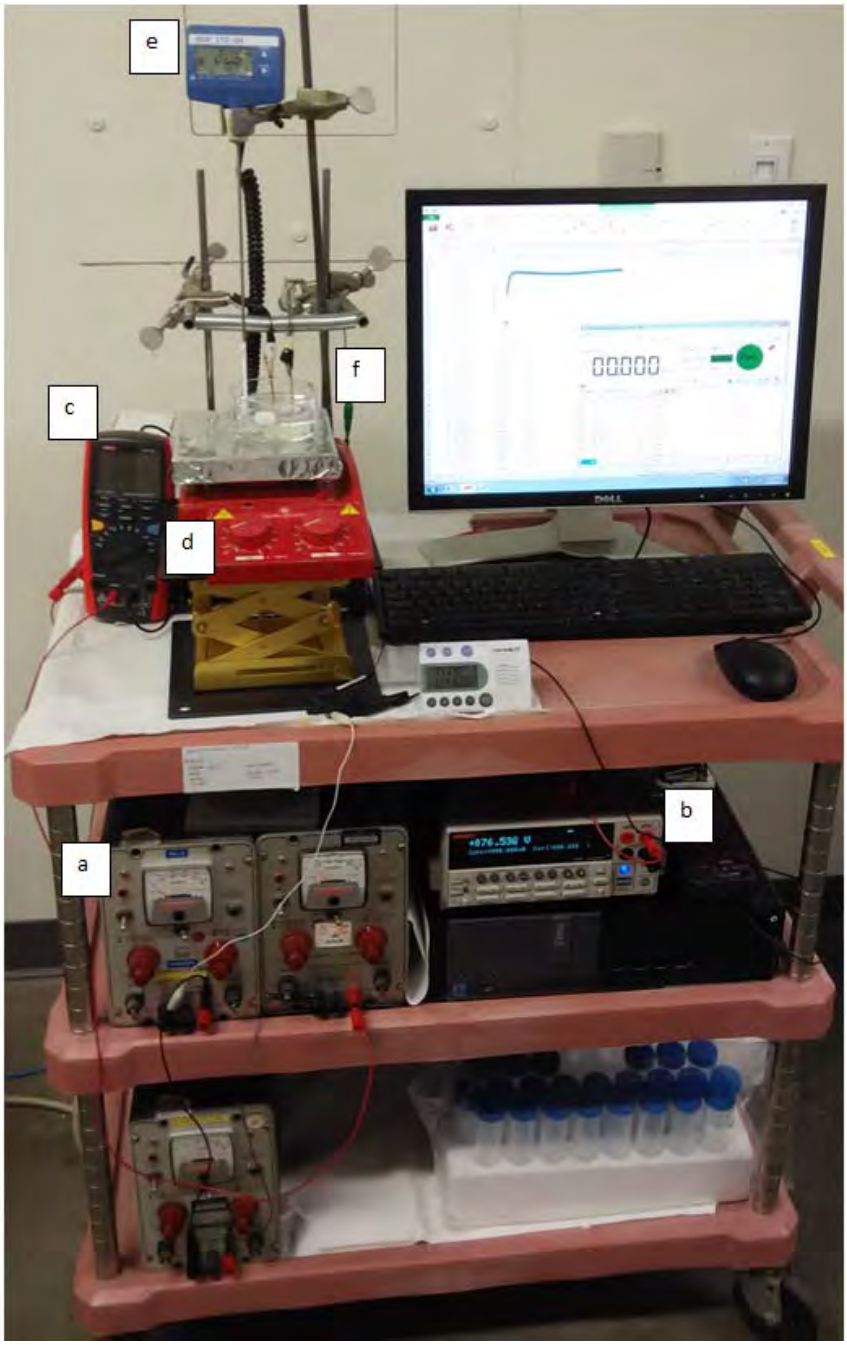

Figure 19. A photograph of the general anodization set up: (a) power supply, (b) multimeter/alternative power source, (c) multimeter, (d) heating plate, (e) temperature controller (f) galvanic cell

The potentials applied were 2.5 V, 7.5 V, and 12.5 V. The anodizing temperatures were 60 °C, 75 °C, and 90 °C and were achieved by heating the electrolyte onto a Sigma–Aldrich hot plate magnetic stirrer equipped with an IKA ETS–D5 temperature controller. Finally, the duration of the anodizations varied from 3 to 10 min. During anodizing, the potential was constantly measured using a Keithley 2400 sourcemeter, and the current was monitored and plotted by a UNI-T UT71B multimeter and the UT71A/B interface program.

In every test, a 100 ml solution was prepared. The solution composition consisted of 50 grams of NaOH dissolved in 100 ml DI water, and every test was contacted into a new solution with a new graphite cathode.

After anodization, the samples were rinsed in DI water to remove the occluded ions, dried under a compressed air stream, and stored in a vacuum chamber (Figure 9).

Finally, the recrystallization of the iron oxide was achieved by annealing for 2 hours in 400°, in a furnace of atmospheric environment with heating and cooling rates of 2 °C/min, as shown in Figure 20.

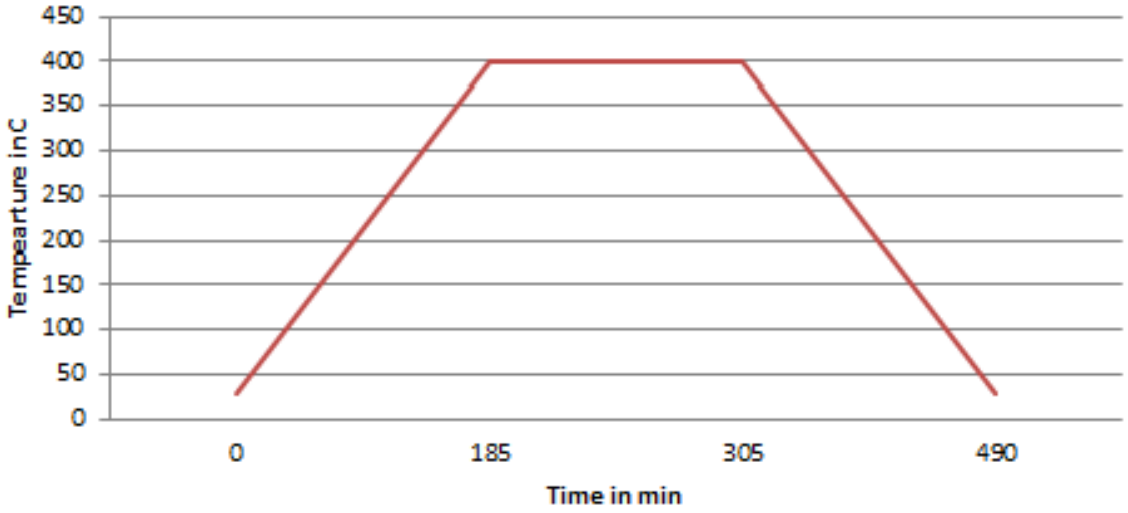

Figure 20. Annealing plot

B. NH_4F-BASED ELECTROLYTE

The main experimental procedure followed in the case of anodizing with a NaOH aqueous solution was repeated in the experiments contacted with a different electrolytic solution, as well. Therefore, the installation of Figure 19 was kept the same and, moreover, all the samples were prepared, dried, stored, and annealed as previously explained. However, there were variations in the anodization conditions that are thoroughly described for each case, separately.

1. 0.50 wt% NH_4F, 3 wt% DI Water

During this technique, the steel plates were anodized in a 100 ml solution composed of 96.77 ml EG, 538.5 mg NH_4F, and 3.23 ml DI water. Experiments were contacted with applied voltages within a range of 10 to 50 V, in temperatures of either 50 °C or 60 °C. The anodization time also varied between 5 and 30 min.

2. 0.37 wt% NH_4F, 1.8 wt% DI Water

Following this anodization method, a solution of 370.4 mg NH_4F and 1.8 ml DI water in 98.2 ml of EG was used and all the specimens were anodized for one hour under constant voltage varying from 20 to 50 V at room temperature.

3. 0.37 wt% NH_4F, 0.9 wt% DI Water

Finally, the next set of anodizations was contacted in a similar solution as the previous one but with a decreased quantity of water. Therefore, 370.4 mg NH4F and 0.9 ml DI water dissolved in 99.1 ml of EG, and steel was anodized inside this solution for 5 or 15 min at room temperature. The main difference in the anodization approach in these experiments was the change of source from constant potential to constant current. Using a Keithley 2400 sourcemeter, anodizations took place under constant current densities between 30 to 85 A/m^2.

Table 6. Summary of the applied anodization methods

Method	Electrolytic solution	Temperature	Potential (volts)	Current density (A/m^2)	Duration
1	50 wt% NaOH in DI water	60 °C, 75 °C, and 90 °C	2.5, 7.5, and 12.5 V	-	3, 5, and 10 min
2	0.50 wt% NH_4F, 3 wt% DI water in EG	50 °C and 60 °C	10, 25,30, 40, and 50 V	-	5, 10, and 30 min
3	0.37 wt% NH_4F, 1.8 wt% DI water in EG	Room temperature (approximately 25 °C)	20, 30, 40, and 50 V	-	1 hour
4	0.37 wt% NH_4F, 0.9 wt% DI water in EG	Room temperature (approximately 25 °C)	-	30, 45, 50, 60, and 85 A/m^2	5 and 15 min

V. RESULTS & DISCUSSION

A. CHARACTERIZATION WITH SEM

SEM analysis of steel plates anodized with 50 wt% NaOH solutions showed that anodization was possible only at elevated temperatures over 75 °C . Nevertheless, the structures of the surface did not obtain any homogenous structure, but instead they appear to have suffered corrosion with a very rough surface, as seen in Figure 21. SEM examination in higher magnification revealed that the surface oxide could be grouped into mainly three morphologies: hexagonal, spherical, and nanoporous channels (Figure 22), and they seem to be unaffected by the alteration of anodizing conditions.

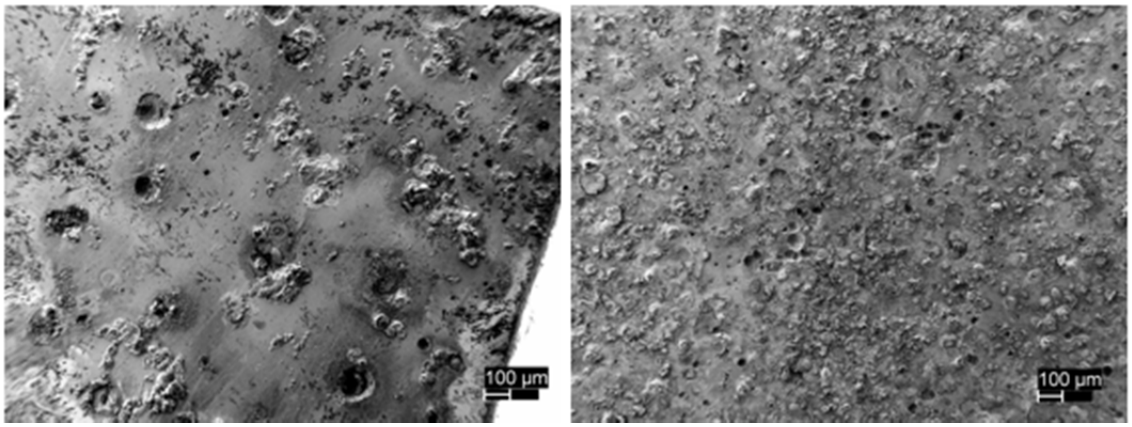

Figure 21. SEM images of anodized steel surfaces under 5 min anodization in 50 wt% NaOH solution under 2.5 V (left) and 12.5V (right) at 75 °C

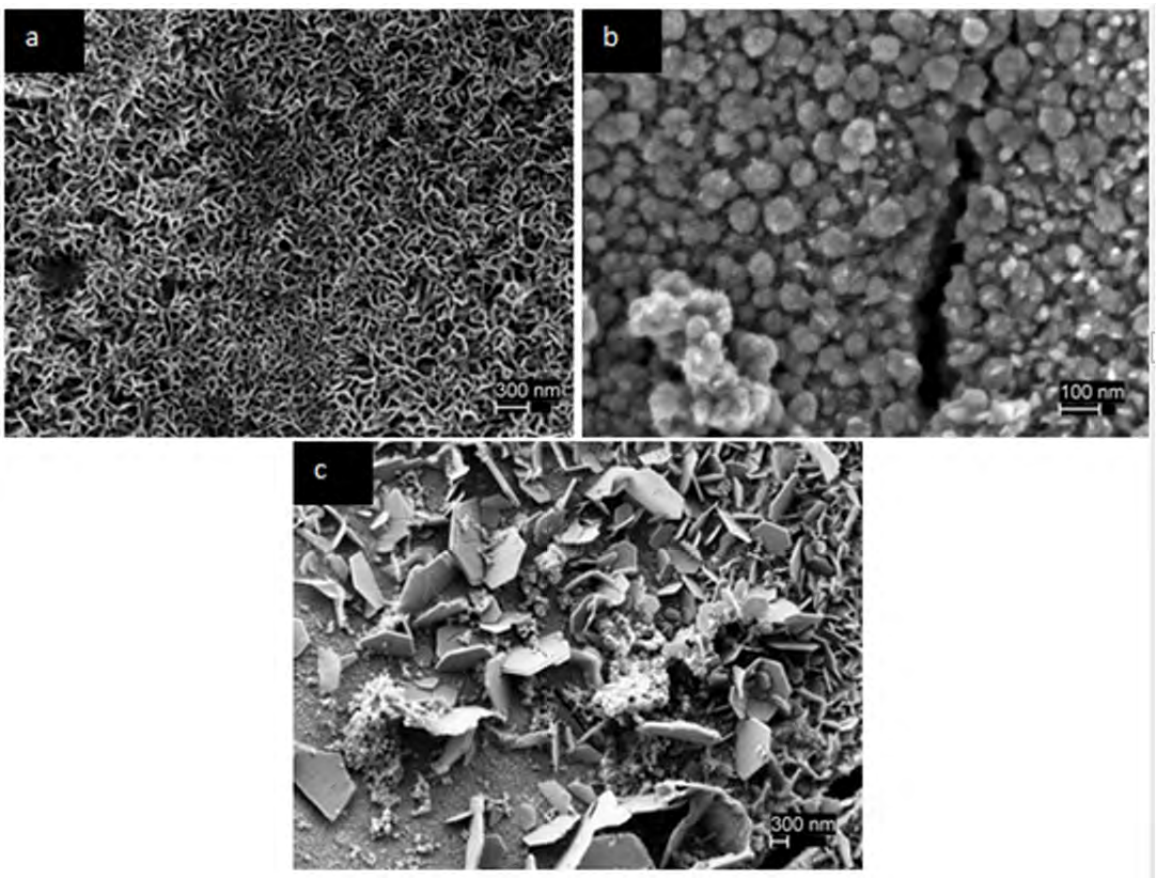

Figure 22. SEM images of (a) nanoporous channels, (b) spherical, and (c) hexagonal crystal structures on anodized steel surfaces under 5 min, 12.5 V anodization in 50 wt% NaOH solution

From these morphologies, the spherical and hexagonal patterns appear on the outside layer of the surface while the nano channels formed within a crater or a pit. An example is shown in Figure 23.

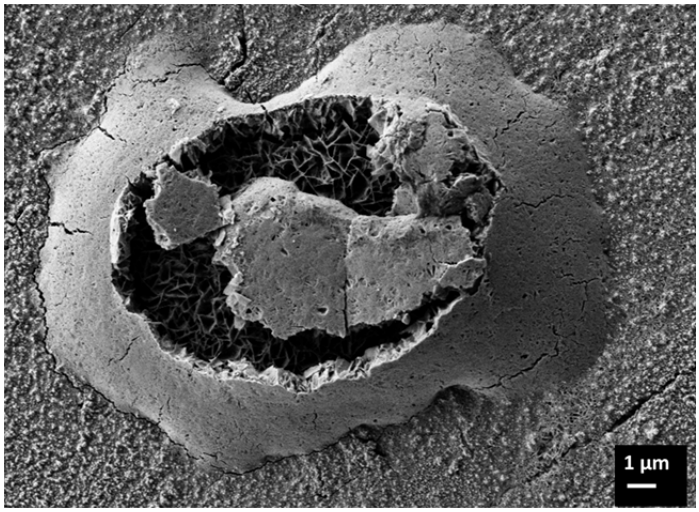

Figure 23. Image of a “collapsed” hump on the surface of a 5 min, 2.5 V, at 90 °C anodized steel in 50 wt% NaOH solution

Due to the highly corroded appearance of the anodized surface resulting from the NaOH solution anodizations and the variations in their oxide morphology, an alternative electrolyte, the 0.50 wt% NH_4F, 3 wt% DI water in EG solution, was examined. Anodizations were performed at a range of 10 to 50 V and the results showed the creation of a severely pitted oxide surface (Figure 24). This large amount of holes in the anodized surface of steel is due to the high water concentration on the solution and the creation of bubbles as the surface of the sample is subjected to the electrochemical anodization. The creation of bubbles and subsequently of holes in the surface is promoted when high potentials are used. Furthermore, anodization duration was kept to 5 min since any attempt made to increase it resulted in a heavily corroded topography (as displayed in Figure 25).

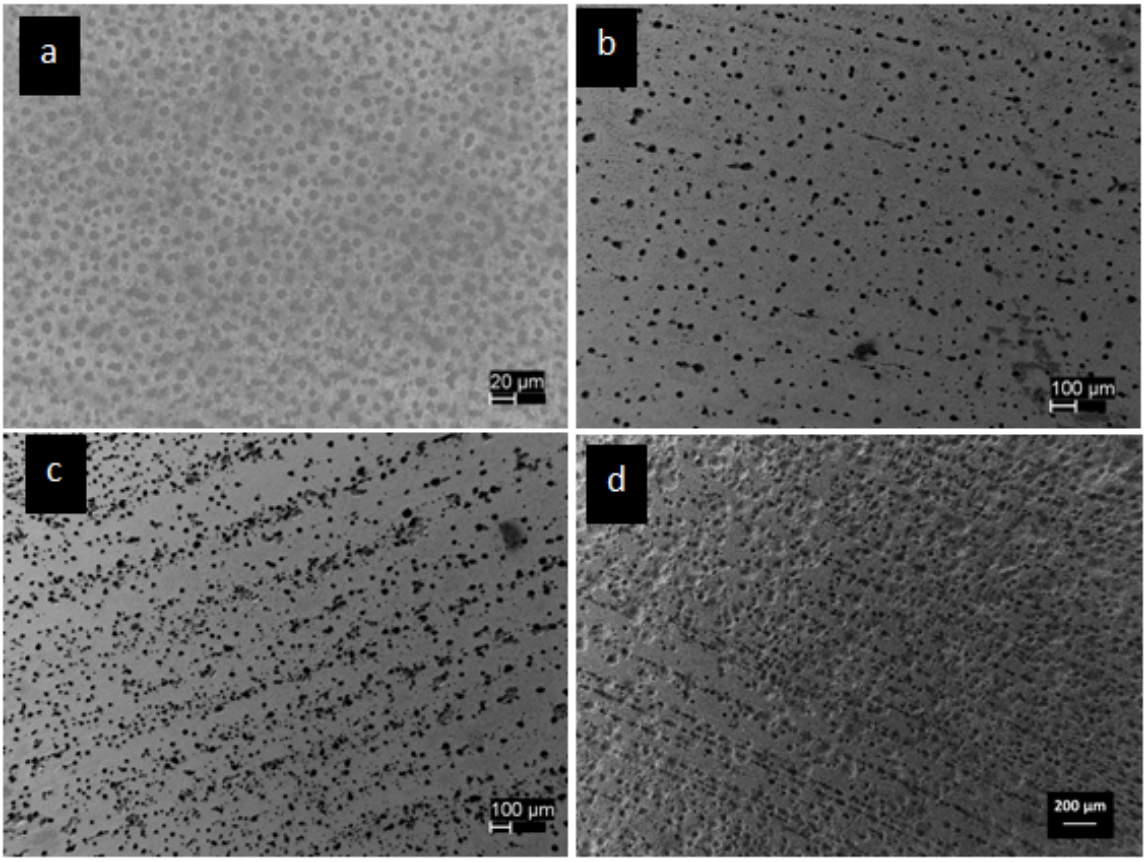

Figure 24. SEM images showing the pitting effect on the surface of anodized HY-80 steel under potentials of (a) 10 V,(b) 25 V, (c) 30 V, and (d) 50 V

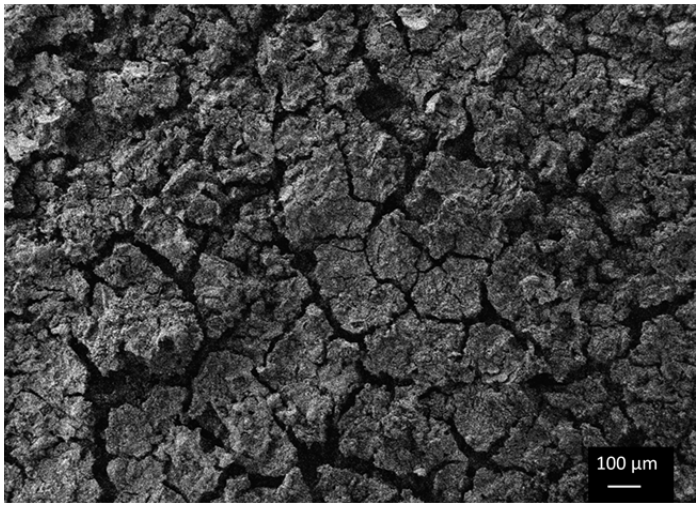

Figure 25. SEM image of steel surface under 10 min, 50 V anodization in 0.50 wt% NH_4F, 3 wt% DI water EG solution at 60 °C

In low potential anodizations, the main structures appearing are 20 nm pores and nano channel like complexes that develop on round patterns (Figure 26). By further increasing the potential, the same two structures continue to appear until 50 V are applied. Above this potential, the topography seems to collapse and the final product shows signs of an amorphous oxide layer (Figure 29). By repeating the experiments at lower temperatures (50 °C), it becomes clear that the construction of nanoporous pits is favored over nano channeling patterns, but the final morphology still remains highly heterogeneous.

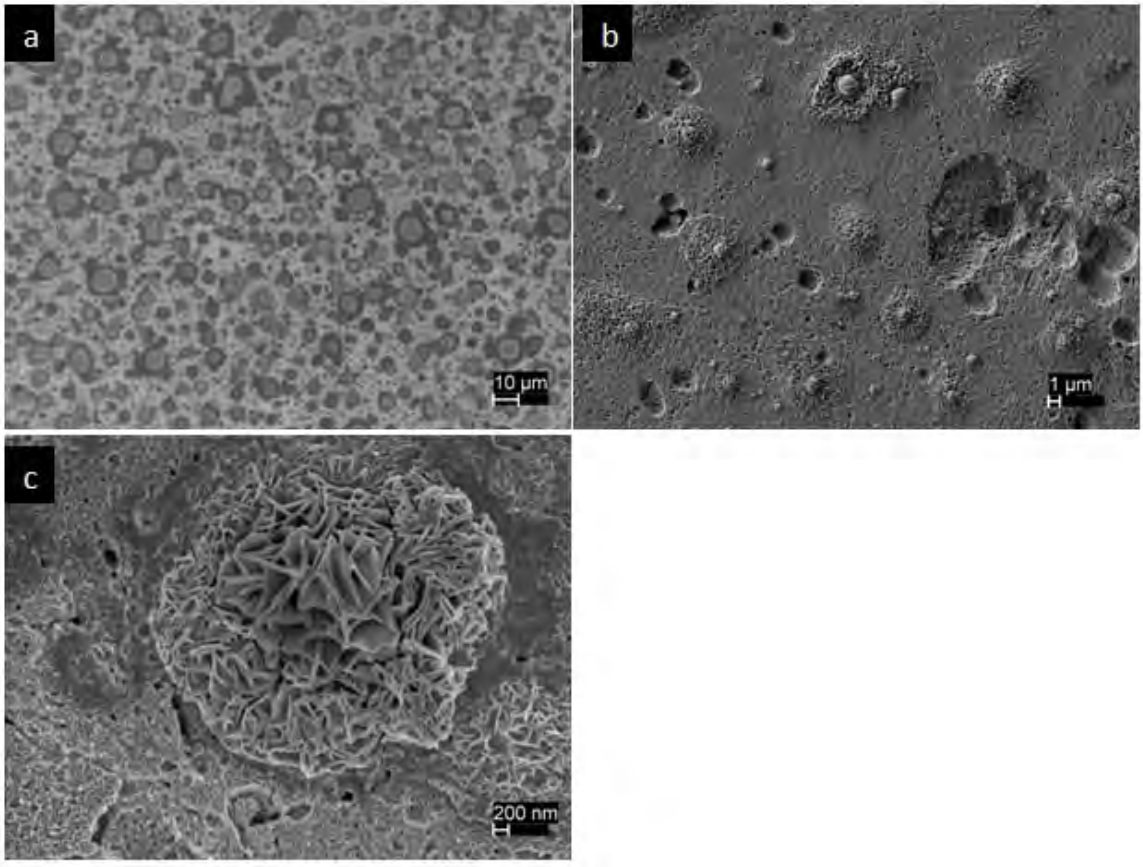

Figure 26. SEM images of anodized sample in 10 V, 60 °C, 0.50 wt% NH_4F, 3 wt% DI water in EG electrolyte under (a) low, (b) medium, and (c) high magnification

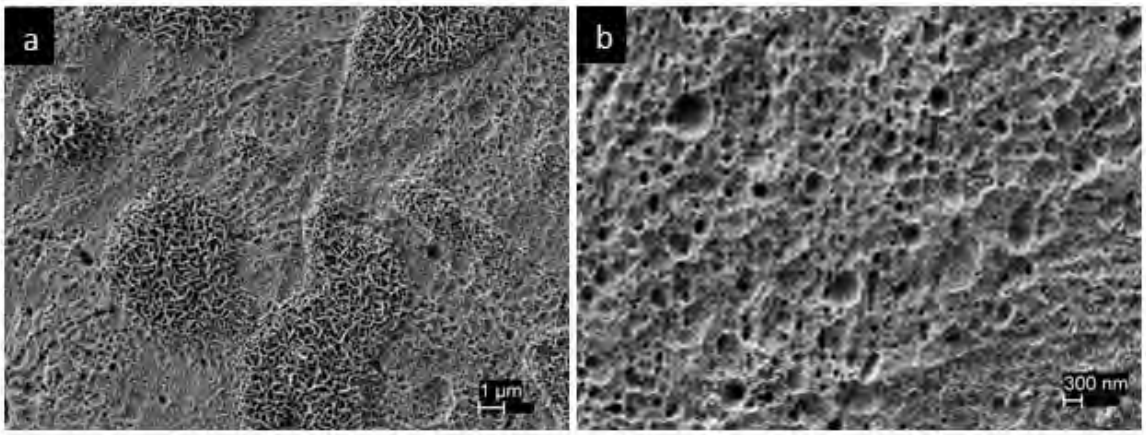

Figure 27. SEM images of anodized sample in 25 V, 60 °C, 0.50 wt% NH_4F, 3 wt% DI water in EG electrolyte under (a) low and (b) high magnification

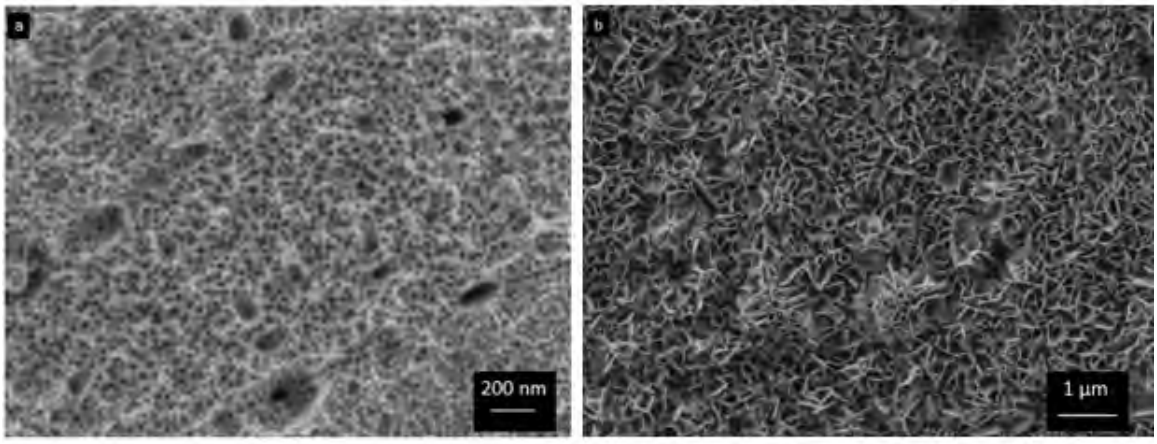

Figure 28. SEM images of anodized sample in 40 V, 60 °C, 0.50 wt% NH_4F, 3 wt% DI water in EG electrolyte focusing on (a) nano porous and (b) nano channeling structure

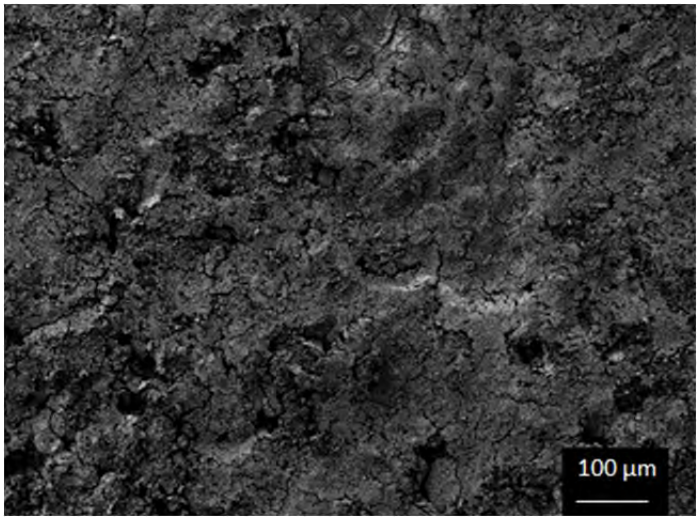

Figure 29. SEM macroscopic images of anodized sample in 50 V, 60 °C, 0.50 wt% NH_4F, 3 wt% DI water in EG electrolyte

In an effort to avoid the extreme surface pitting due to the high concentration of water in the previous electrolyte, a new solution was used with less concentration in NH_4F and water. The experiments on 0.37 wt% NH_4F, 1.8 wt% DI water EG solution proved that a nanoporous oxide layer is produced with this electrolyte, as seen in Figures 30 and 31, between the range of 20 to 30 V. Initially 20 nm diameter pits were developed on the surface of the steel, which coalesced together to form larger pores as anodization continued. This progress of the oxide layer is relatively slow in low potential anodizations compared to the one appearing in applied potential of 40 V or more. As a result of it, when conducting anodizations under a voltage of 20 V, the average diameter of the constructed pores was 150 nm, whereas for 30 V, the resulted pores were of approximately 120 nm diameters. In even higher voltages, though, the evolution of the oxide happens so fast that it totally consumes the initially developed topography, as Figures 32 and 33 indicate.

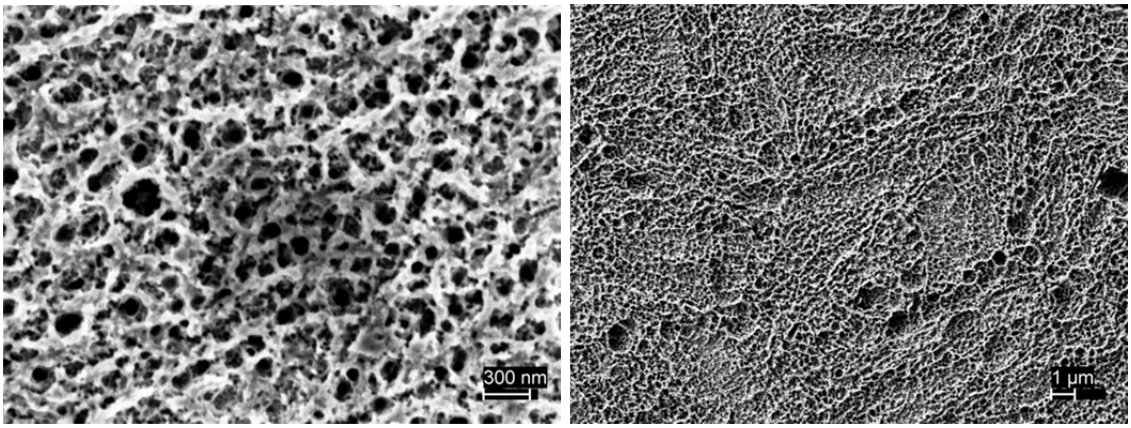

Figure 30. SEM images on high (left) and low (right) magnification of nanoporous structure under 1 h anodization in a 0.37 wt% NH_4F, 1.8 wt% DI water EG solution on 20 V at 25 °C

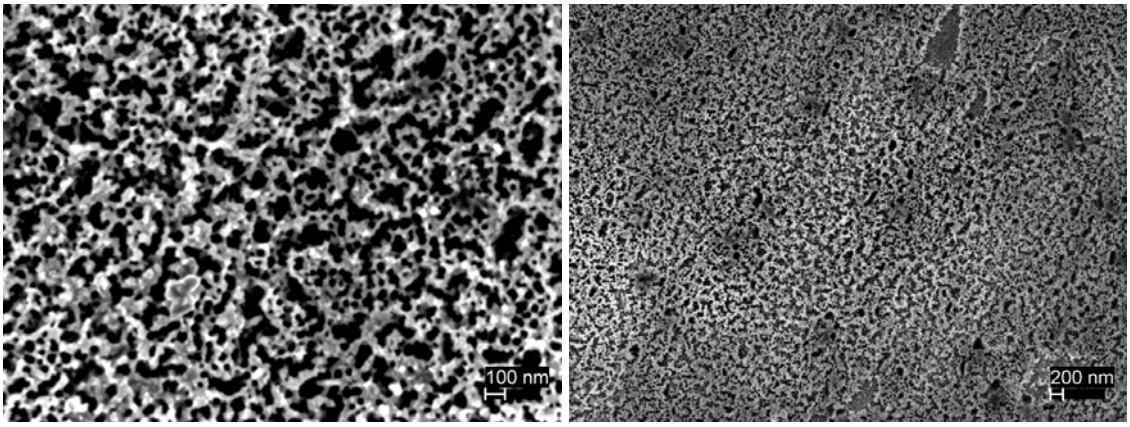

Figure 31. SEM images on high (left) and low (right) magnification of nanoporous structure under 1 h anodization in a 0.37 wt% NH_4F, 1.8 wt% DI water EG solution on 30 V at 25 °C

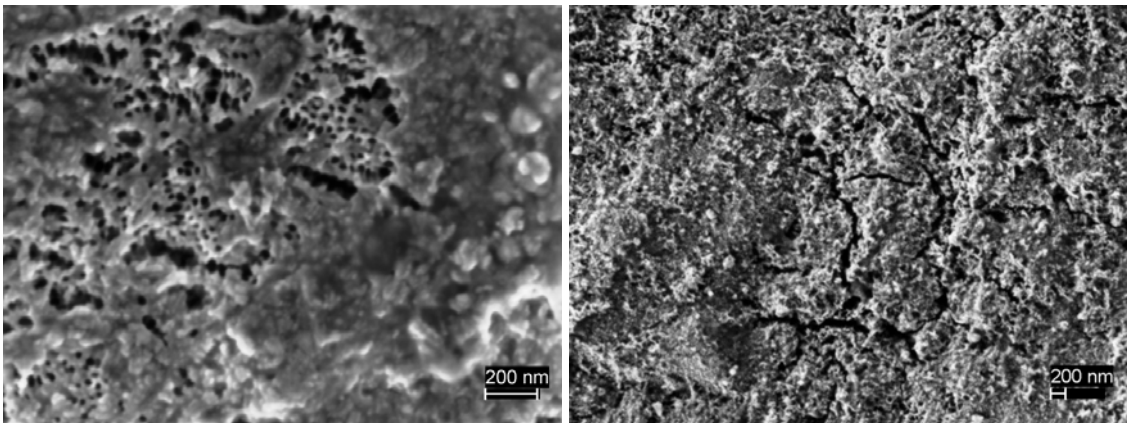

Figure 32. SEM images on high (left) and low (right) magnification of nanoporous structure under 1 h anodization in a 0.37 wt% NH_4F, 1.8 wt% DI water EG solution on 40 V at 25 °C

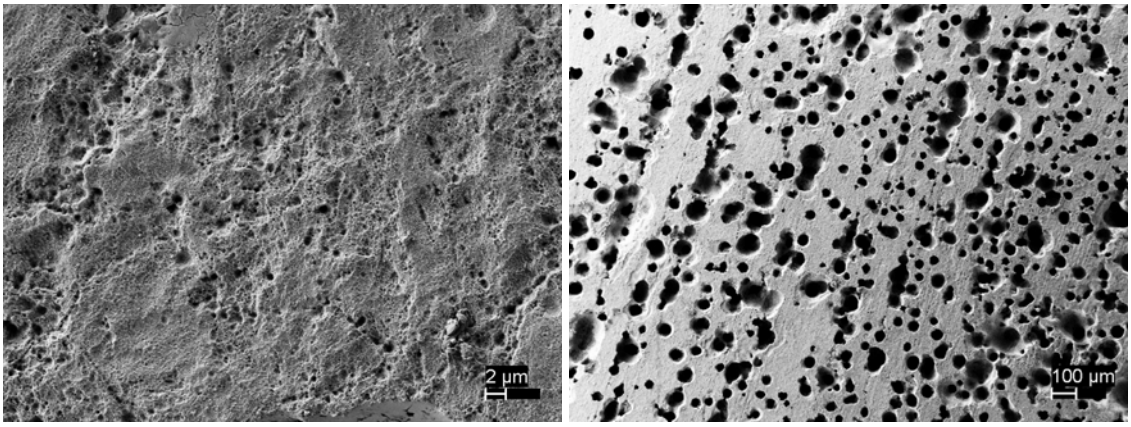

Figure 33. SEM images on high (left) and low (right) magnification of nanoporous structure under 1 h anodization in a 0.37 wt% NH_4F, 1.8 wt% DI water EG solution on 50 V at 25 °C

By further decreasing the amount of water contained in the electrolyte and by changing the anodization approach from potentiostatic to galvanostatic, it was possible to achieve uniform distribution of nanoporous oxide morphologies. The secondary electron images in Figures 34 and 35 indicate a self-oriented nanoporous anodic film created with current densities between 30 and 85 A/m^2. Cylindrical nanopores of 20 nm average diameter were initially developed and merged together to form larger pores whose diameter was measured to be

approximately 90 nm regardless of the current density in the anodizing range used.

A thorough SEM examination revealed very closely spaced porous structures along the scratches (polishing lines) on these surfaces, and a similar structure is observed along grain boundaries as well in Figure 37.

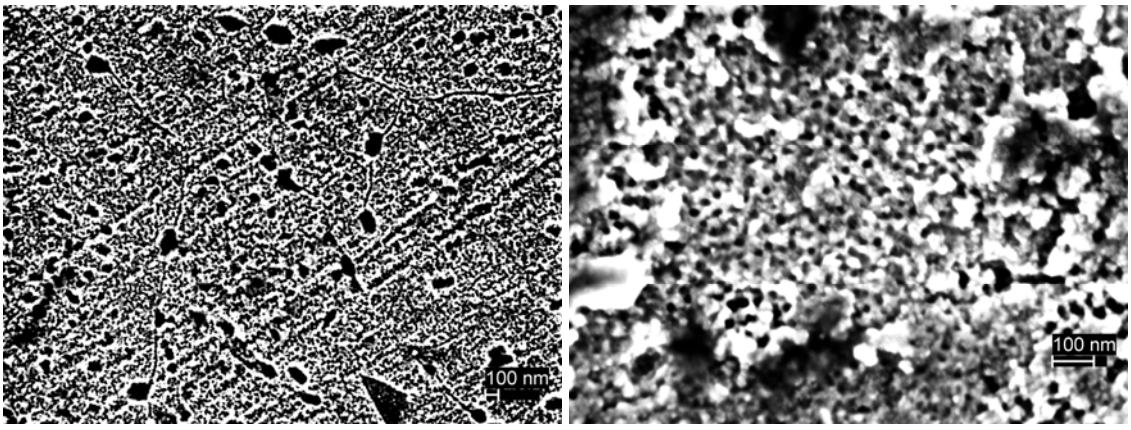

Figure 34. SEM images of nanoporous structure under 5 min (left) or 15 min (right) anodization in a 0.37 wt% NH_4F, 0.9 wt% DI water EG solution with applied current density of 30A/m^2 at 25 °C

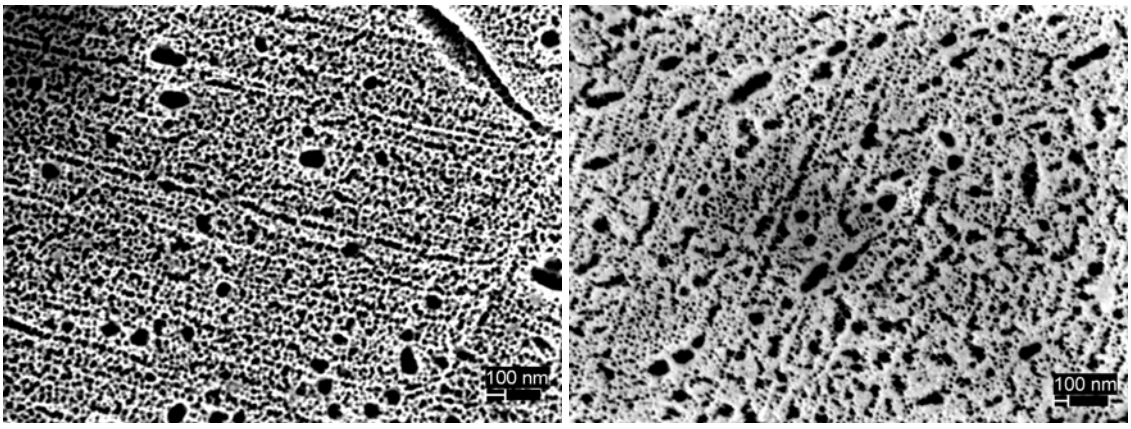

Figure 35. SEM images of nanoporous structure under 5 min (left) or 15 min (right) anodization in a 0.37 wt% NH_4F, 0.9 wt% DI water EG solution with applied current density of 45A/m^2 at 25 °C

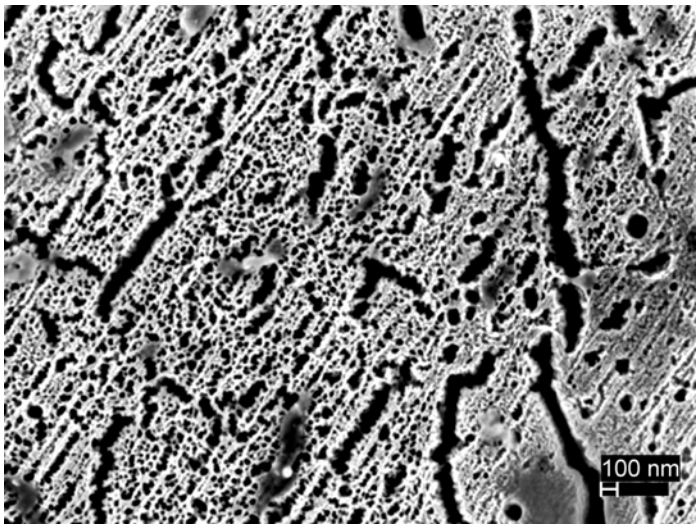

Figure 36. SEM images of nanoporous structure under 5 min anodization in a 0.37 wt% NH4F, 0.9 wt% DI water EG solution with applied current density of 85A/m^2 at 25 °C

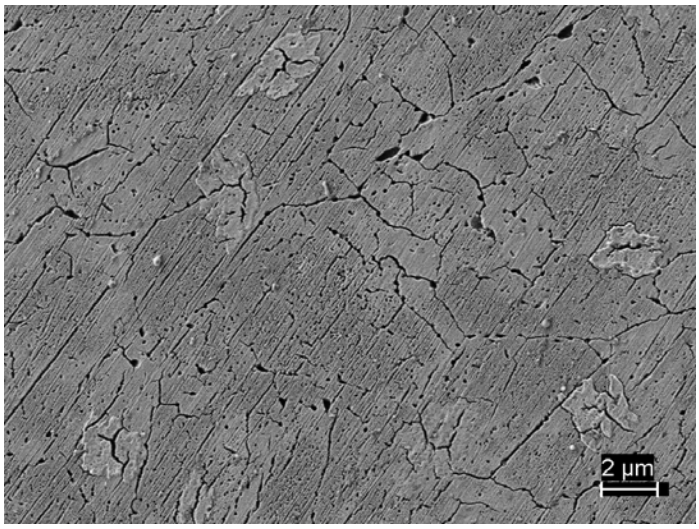

Figure 37. SEM image on a 5 min anodized surface under 85A/m^2

Finally, further examination revealed that by increasing the anodization time, the growth of the homogeneous nanoporous pattern is replaced with large regions of oxide growing over the previous nanoporous layer. This is a procedure similar to the one described in the 1.8wt% solutions that evolves rapidly under higher applied currents (Figure 38).

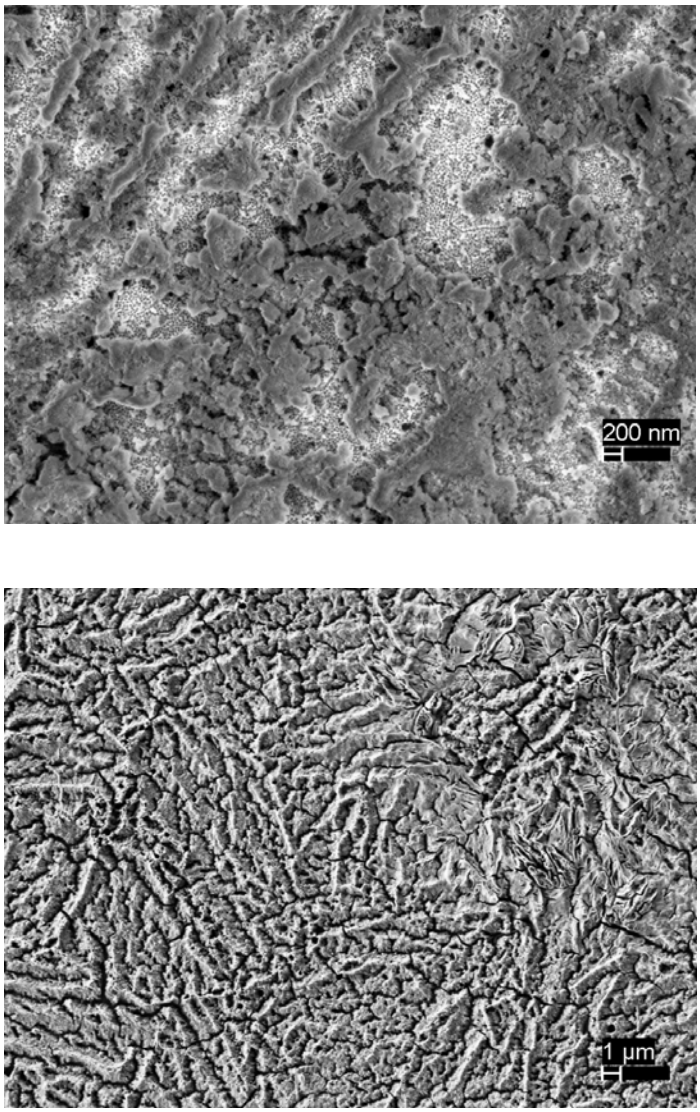

Figure 38. SEM images on a lower magnification of samples anodized for 15 min at 60 A/m^2 (top) and 85A/m^2 (bottom)

The morphological features of the anodized surfaces studied here can be summarized as follows:

- Anodization in NaOH solutions creates heterogeneous and highly corroded surfaces. The surface oxide consists of mainly three morphologies: the hexagonal and spherical patterns, which appear on the outside layer of the surface, and the nanoporous channels, which are formed on the steel substrate.
- In EG solutions of 0.50 wt% NH_4F, 3 wt% DI water, a severely pitted surface was obtained. In the voltage range of 10–40 V, two main morphologies appear: 20 nm porous topographies and nano channel like complexes that develop on cyclical patterns. However,

for potentials greater than 50 V, the surface shows signs of an amorphous oxide layer.

- Anodizations in EG solutions of 0.37 wt% NH_4F, 1.8 wt% DI water between 20–30 V create a homogeneous nanoporous oxide layer with an average pore diameter varying from 120 to 150 nm depending on the anodization voltage. Nevertheless, when the anodization potential increases more than 40 V, the oxide will grow and consume the previous layer
- While in EG solutions of 0.37 wt% NH_4F, 0.9 wt% DI water, galvanostatic anodization self-oriented nanoporous anodic film with an average porous diameter of 90 nm are produced only between current densities from 30 to 85 A/m^2. Moreover, when anodization time exceeds 15 min, the oxide grows over the previous nanoporous layer.

B. GROWTH KINETICS OF NANOPOROUS ANODIC FILMS

SEM analysis showed that homogeneous nanoporous structures can be formed on HY-80 steels in an EG containing ammonium fluoride and water electrolyte under both potentiostatic and galvanostatic anodization. In order to study the kinetics over the creation and growth of this nanoporous structure, the current density and the potential were constantly monitored and plotted.

In case of potentiostatic anodization, a typical current densities versus time graph obtained is plotted in Figure 39. There are many similarities between the current density transient obtained with the one observed in the anodization of iron [25], which can be described in the following three stages. In order to clearly see the three stages, three plots with appropriate axes scales for the same set of data were shown in this figure.

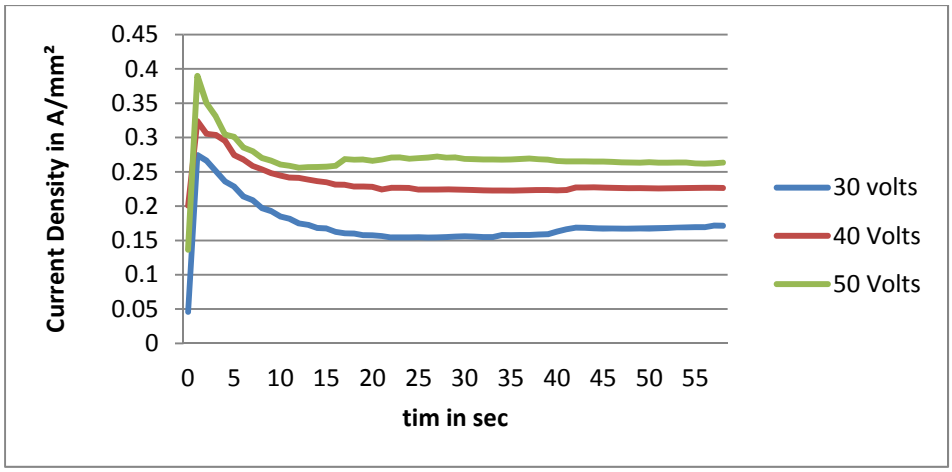

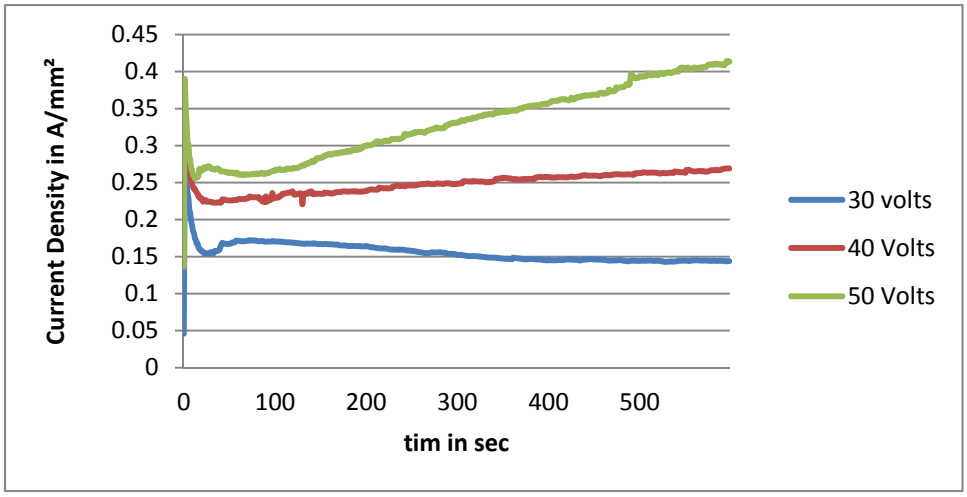

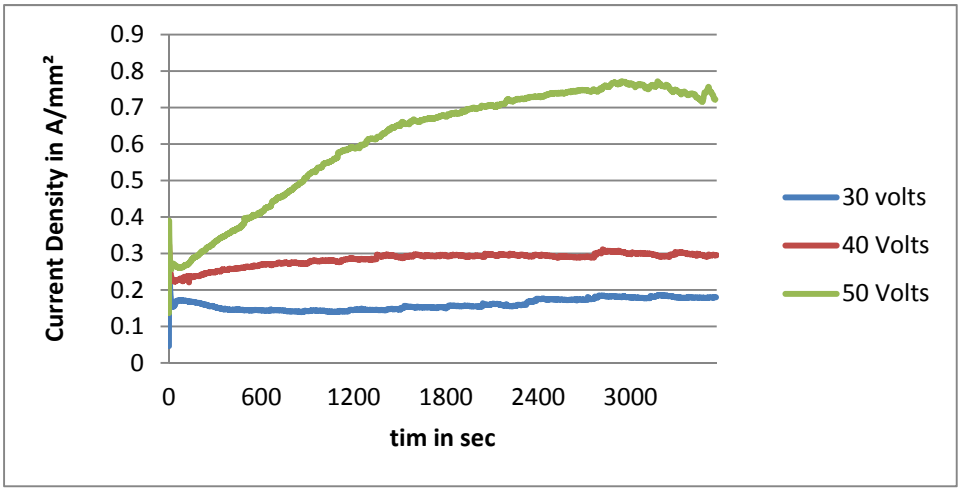

Figure 39. Current density versus time curve recorded during anodization in 0.37 wt% NH_4F, 1.8 wt% DI water EG solution at 25 °C during various time intervals

At the first stage, current density decreases rapidly within 20 seconds. This drop is because of the fast growth of an oxide layer on a steel plate in an EG solution containing fluorides and water, which via the overall chemical reaction of equation (8), subsequently leads to a resistance increase. At this point, the initial 20 nm diameter pits are formed on the oxide surface, which with time gradually merge into larger pores due to the following chemical dissolution of the oxide.

$$Fe_2O_3 + 12F^- + 6H^+ \rightarrow 2\left[FeF_6\right]^{3-} + 3H_2O \quad (8)$$

At the second stage, a slow increase of current density is observed, which relates to the decreased surface resistance of the oxide layer via gradual formation of the metal-fluoride complex anion according to equation (8).

Finally, in the third stage, the current density reaches a constant value, which implies that a dynamic equilibrium between the rate of oxide formation and that of the oxide dissolution has been achieved.

The observed electrochemical evolution was explained in the model proposed by Xie et al. [25] of the formation of iron oxide nanotubes in Fe foils. When anodization begins, subsequent to the formation of an oxide layer, fine pits are formed due to the localized dissolution of the oxide layers by F^- ion. Due to the barrier level being thin at the bottom of the pore while the electric field intensity across the remaining barrier layer is high, the pore becomes wider and deeper. The presence of substantial amounts of H^+ in solution greatly enhances the dissolution process and thus the fine pore coalescence and growth. As the larger pores become deeper and deeper, a highly oriented nanoporous structure is established.

In the case of 50 V applied voltage, an anomaly to the previous described curve is reported. After the initial rapid drop in current density, a constant increase is observed for 45 min followed by a decrease in current density. The explanation behind this phenomenon is that because of the high potential, a

dynamic equilibrium between oxide growth and dissolution is never established and the dissolution process is favored over the oxide formation.

To study the electrochemical behavior of the anodic film during the formation of the iron-oxide nanoporous structure in galvanostatic anodization, the potential densities versus time graphs were plotted, as seen in Figures 40 and 41. Since the oxide creation and growth are similar to the process described above, similar behavior is obtained. Again, after the initiation of oxidation, the fast growth of the oxide leads to resistance increase, which subsequently causes the potential to increase almost linearly. The fine pits are making their appearance and they merge together through chemical dissolution forming larger pores as equation (8) implies. As the pores deepen, the thickness of the barrier layer decreases, and the voltage needed for driving the same current decreases accordingly. After a period of adjustment, a steady state formation voltage is obtained. This stage lasts from one to three minutes depending on the anodization current density applied, where the samples under higher current densities reach the equilibrium condition sooner. For particular values of applied densities (such as 45 A/m^2 or lower), the rates of oxidation and dissolution can balance each other exactly right after the voltage increase and a steady state can eventually be reached with barrier layer thickness and voltage remaining constant with time thereafter [45].

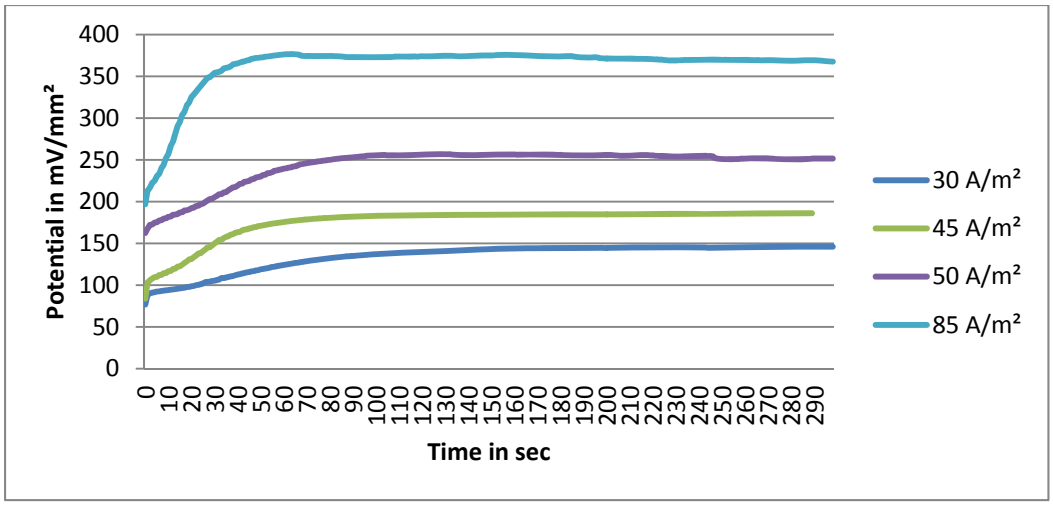

Figure 40. Potential density versus time curve recorded during 5 min anodization in 0.37 wt% NH_4F, 0.9 wt% DI water EG solution at 25 °C

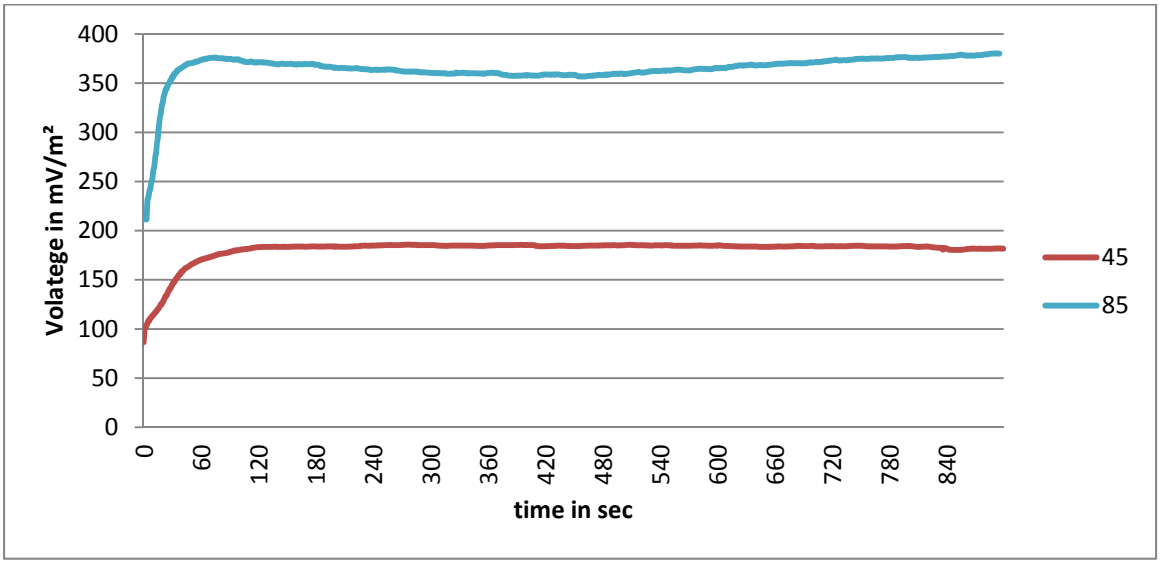

Figure 41. Potential density versus time curve recorded during 15 min anodization in 0.37 wt% NH_4F, 0.9 wt% DI water EG solution at 25 °C

C. CHARACTERIZATION WITH EDS

Initially EDS was used in an effort to identify the difference between the two main structures appearing on the surface of anodized steels in NaOH solutions. EDS analysis revealed that the spherical structured oxide included

larger amounts of oxygen than the hexagonal crystal shaped oxides, as indicated in Figures 42 and 43 and Tables 7 and 8. In spite of the fact that EDS is a useful method to identify the chemical composition of a specimen, in this particular case the relatively small thickness of the constructed oxide layer affected the measurements as the electron interaction volume contained the surface oxide as well as the underlying alloy. The characteristic X-rays from the substrate layer of HY-80 interfered with those that were emitted from the surface and, as a result, Fe appeared to be the predominant element, even in structures where the ratio between oxygen and iron atoms was expected to be different.

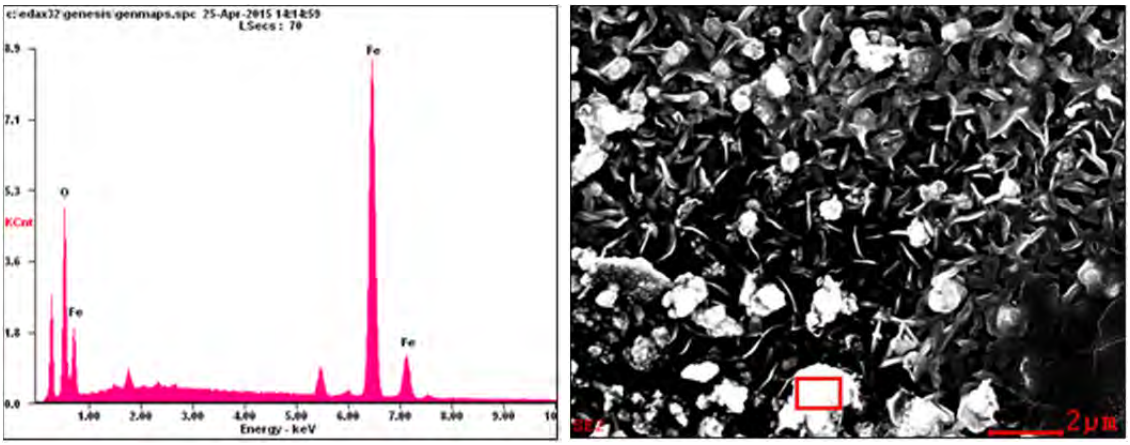

Figure 42. EDS spectrum from the spherical structure oxide on anodized steel surface after 5 min in a 50 wt% NaOH solution with applied voltage of 2.5 V at 75 °C

Table 7. EDS quantitative analysis showing weight and atomic number percent of elements in anodized steel area of Figure 42

Element	**Wt%**	**At%**
Oxygen (O)	13.38	35.02
Iron (Fe)	86.62	64.98
Matrix	Correction	ZAF

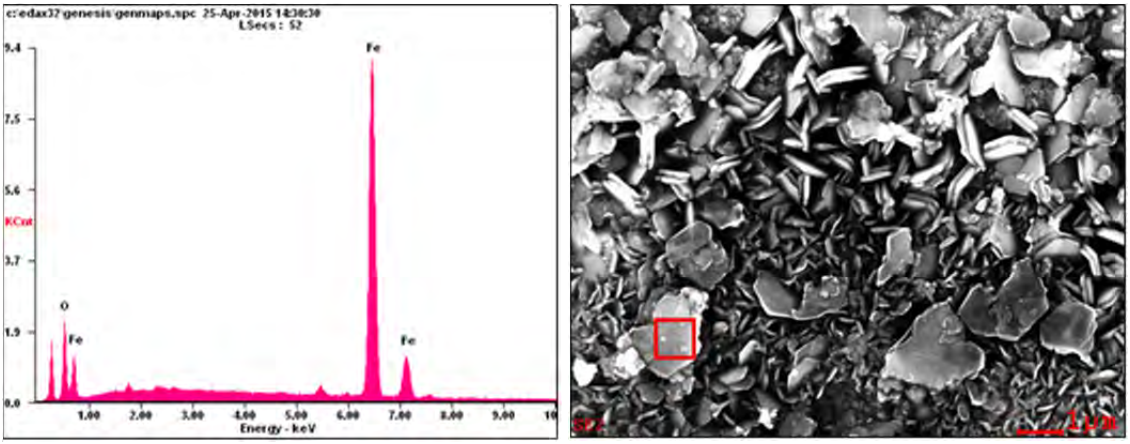

Figure 43. EDS spectrum from the hexagonal structure oxide on anodized steel surface after 5 min in a 50 wt% NaOH solution with applied voltage of 2.5 V at 75 °C

Table 8. EDS quantitative analysis showing weight and atomic number percent of elements in anodized steel area of Figure 43

Element	**Wt%**	**At%**
Oxygen (O)	06.06	18.37
Iron (Fe)	93.94	81.63
Matrix	Correction	ZAF

EDS characterization proved to be inconclusive also in the case of anodized steels in 0.37 wt% NH_4F EG with the constructed oxide appearing to consist of Fe from 80% to 90%, as shown in Figures 44 and 45 and Tables 9 and 10.

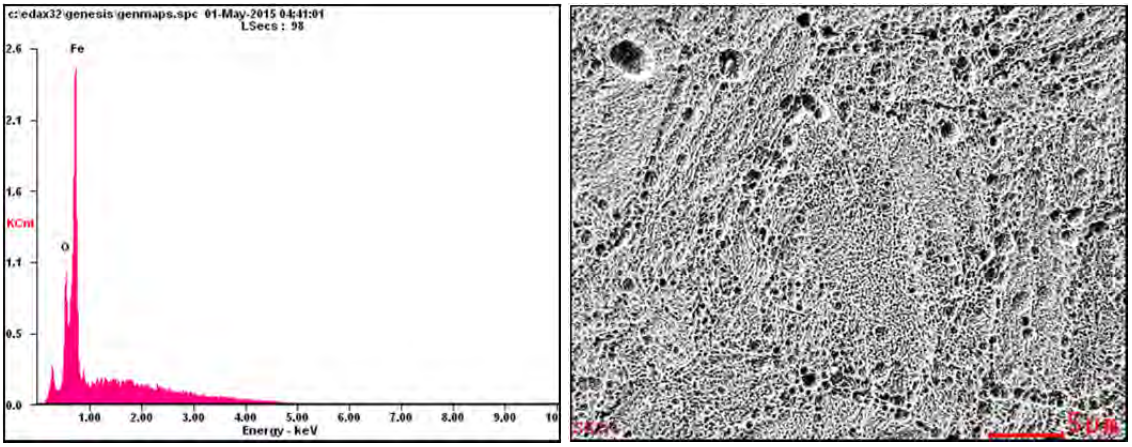

Figure 44. EDS spectra from anodized steel after 1 hour in a 0.37 wt% NH_4F, 1.8 wt% DI water EG solution with applied voltage of 20 V at room temperature

Table 9. EDS quantitative analysis showing weight and atomic number percent of elements in the Figure 44 anodized steel

Element	**Wt%**	**At%**
Oxygen (O)	05.61	17.19
Iron (Fe)	94.39	82.81
Matrix	Correction	ZAF

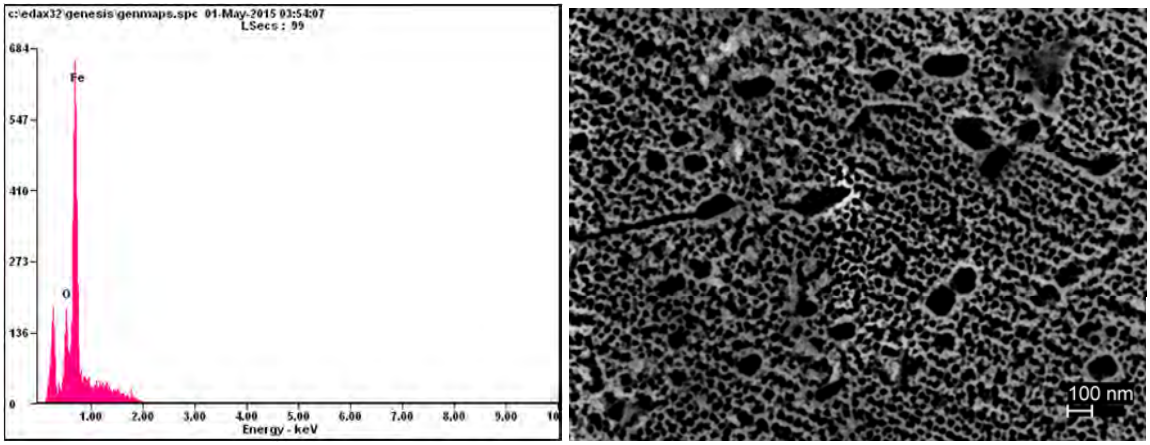

Figure 45. EDS spectra from anodized steel after 5 min in a 0.37 wt% NH_4F, 0.9 wt% DI water EG solution with applied current density of 40A/m^2 at room temperature

Table 10. EDS quantitative analysis showing weight and atomic number percent of elements in the Figure 45 anodized steel

Element	Wt%	At%
Oxygen (O)	02.89	09.40
Iron (Fe)	97.11	90.60
Matrix	Correction	ZAF

D. CHARACTERIZATION WITH XRD

X-ray diffractometry was used in every sample to investigate the type of surface oxides formed during anodization and the effects that the annealing process had on them. The following figures show the X-ray diffraction patterns of the anodized iron oxides for different treatments.

XRD patterns from samples anodized in NaOH solutions showed peaks corresponding to martensitic steel, wustite, $Fe_{0.93}O$, and magnetite, Fe_3O_4. As the applied voltage, anodization time, or temperature increased, so did the fraction of magnetite. However, after the annealing process, magnetite peaks reduced their intensity (nearly disappeared), suggesting that all magnetite is converted to wustite, as can be seen in Figures 46 and 47.

In case of anodization in EG solutions of 0.50 wt% NH_4F, 3 wt% DI water, the only XRD peaks appearing are of martensitic steel and wustite, $Fe_{0.93}O$. After annealing the oxide, $Fe_{0.93}O$ is converted into Fe_2O_3. In low voltage anodizations (such as the 30 V anodization appearing in Figure 48), the structure of the oxide is maghemite, which has a cubic crystal structure. As the anodization voltage increases, the phase is hematite, Fe_2O_3, with a trigonal hexagonal structure (XRD is shown in Figure 49 after 50 V anodization).

In the 0.37 wt% NH_4F, 1.8 wt% DI water EG solutions, again before annealing, only XRD peaks for martensitic steel and wustite are visible; however, after heat treatment, a very small amount of magnetite is also observed as a secondary phase, and the experiments conducted between applied voltages of 20 V and 50 V did not show any significant change in the constructed oxide (Figure 50).

Finally, in the case of the 5 min galvanostatic anodization in 0.37 wt% NH_4F, 0.9 wt% DI water EG solutions, even after annealing, the only peaks observed belong to wustite ($Fe_{0.93}O$) and to martensitic steel. Furthermore, by changing the anodization parameters of the applied current density within a range of 30 to 85 A/m^2 and of the anodization time from 5 to 15 min, the oxide layer structure remains unaffected (Figure 51).

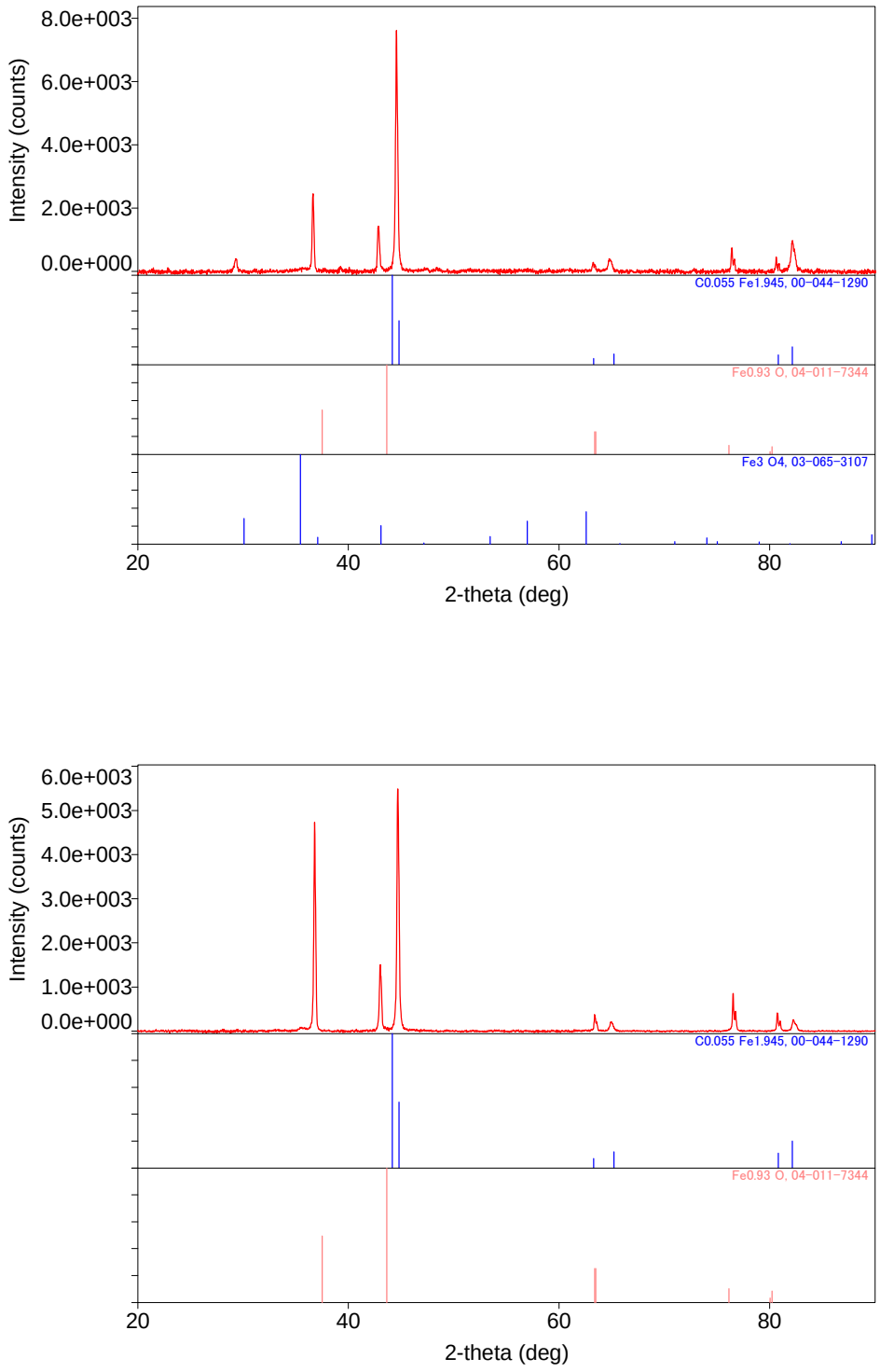

Figure 46. XRD patterns of the iron oxide created after 5 min anodization in 7.5 V, 75 °C, in a 50 wt% NaOH solution before (top) and after (bottom) annealing

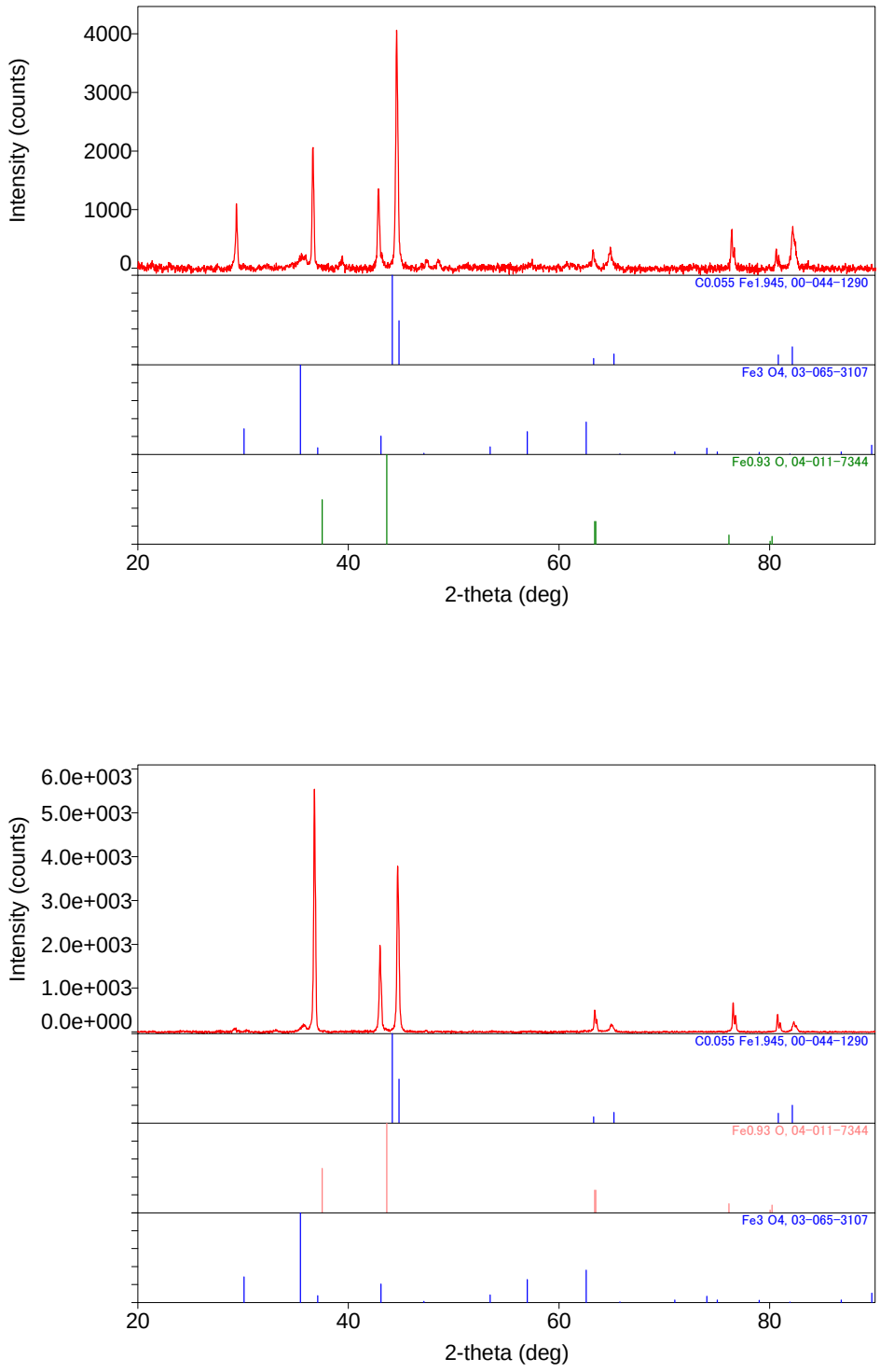

Figure 47. XRD patterns of the iron oxide created after 5 min anodization in 12.5 V, 75 °C, in a 50 wt% NaOH solution before (top) and after (bottom) annealing

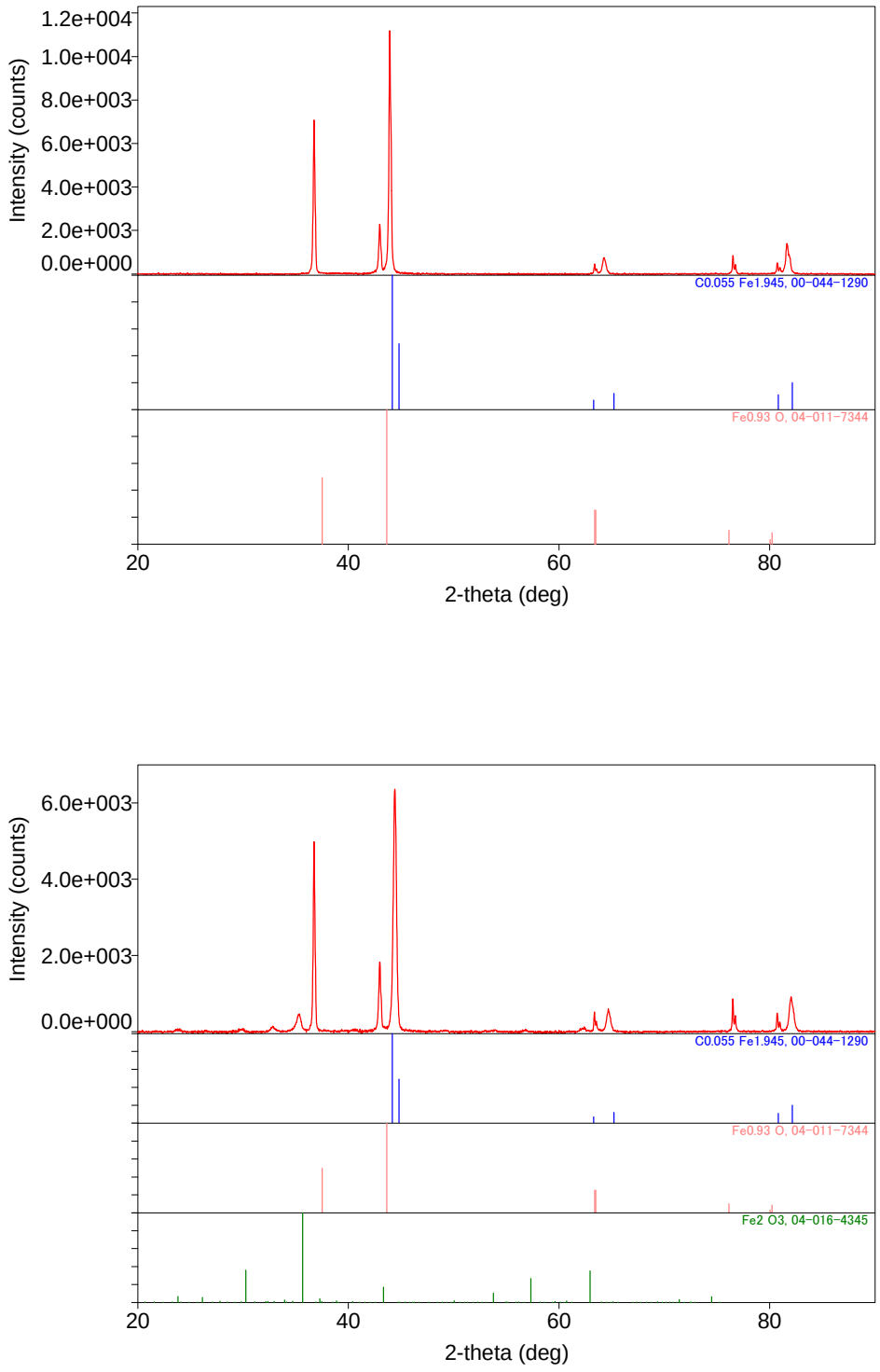

Figure 48. XRD patterns of the iron oxide created after 5 min anodization in 30 V, 50 °C, in a 0.50 wt% NH4F, 3 wt% DI water EG solution before (top) and after (bottom) annealing

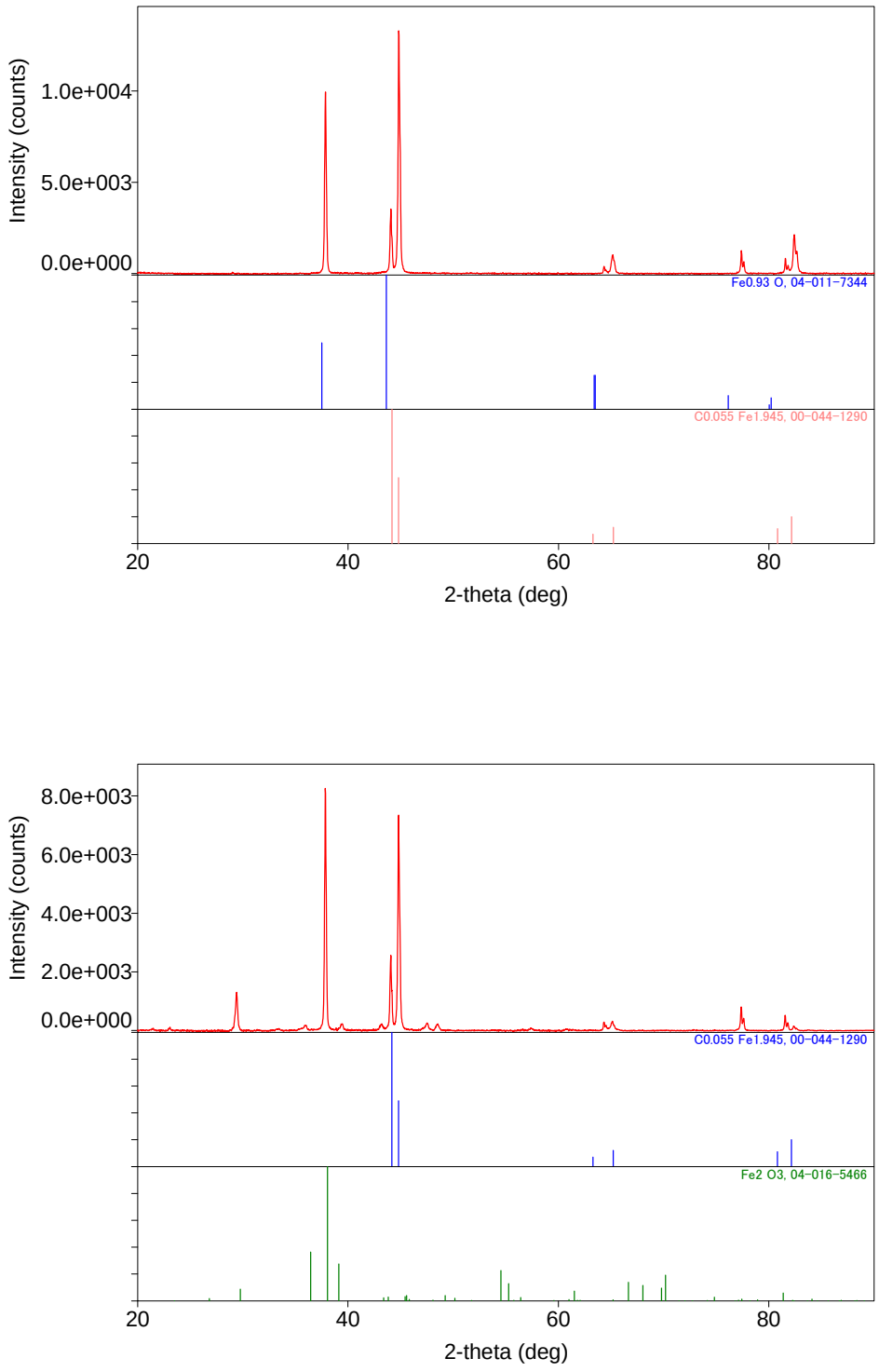

Figure 49. XRD patterns of the iron oxide created after 5 min anodization in 50 V, 50 °C, in a 0.50 wt% NH4F, 3 wt% DI water EG solution before (top) and after (bottom) annealing

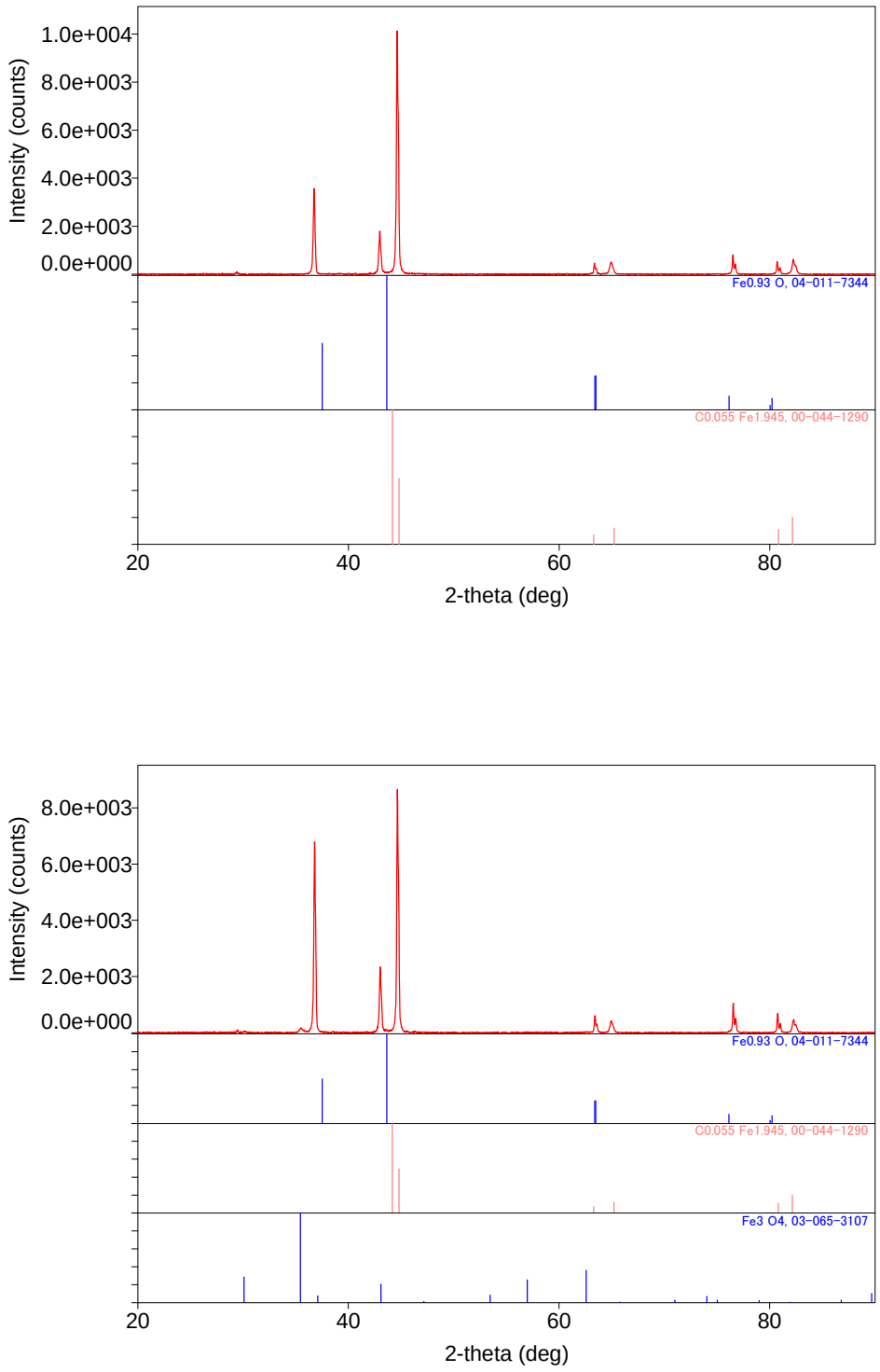

Figure 50. XRD patterns of the iron oxide created after 60 min anodization in 30 V, 25 °C, in a 0.37 wt% NH4F, 1.8 wt% DI water EG solution before (top) and after (bottom) annealing

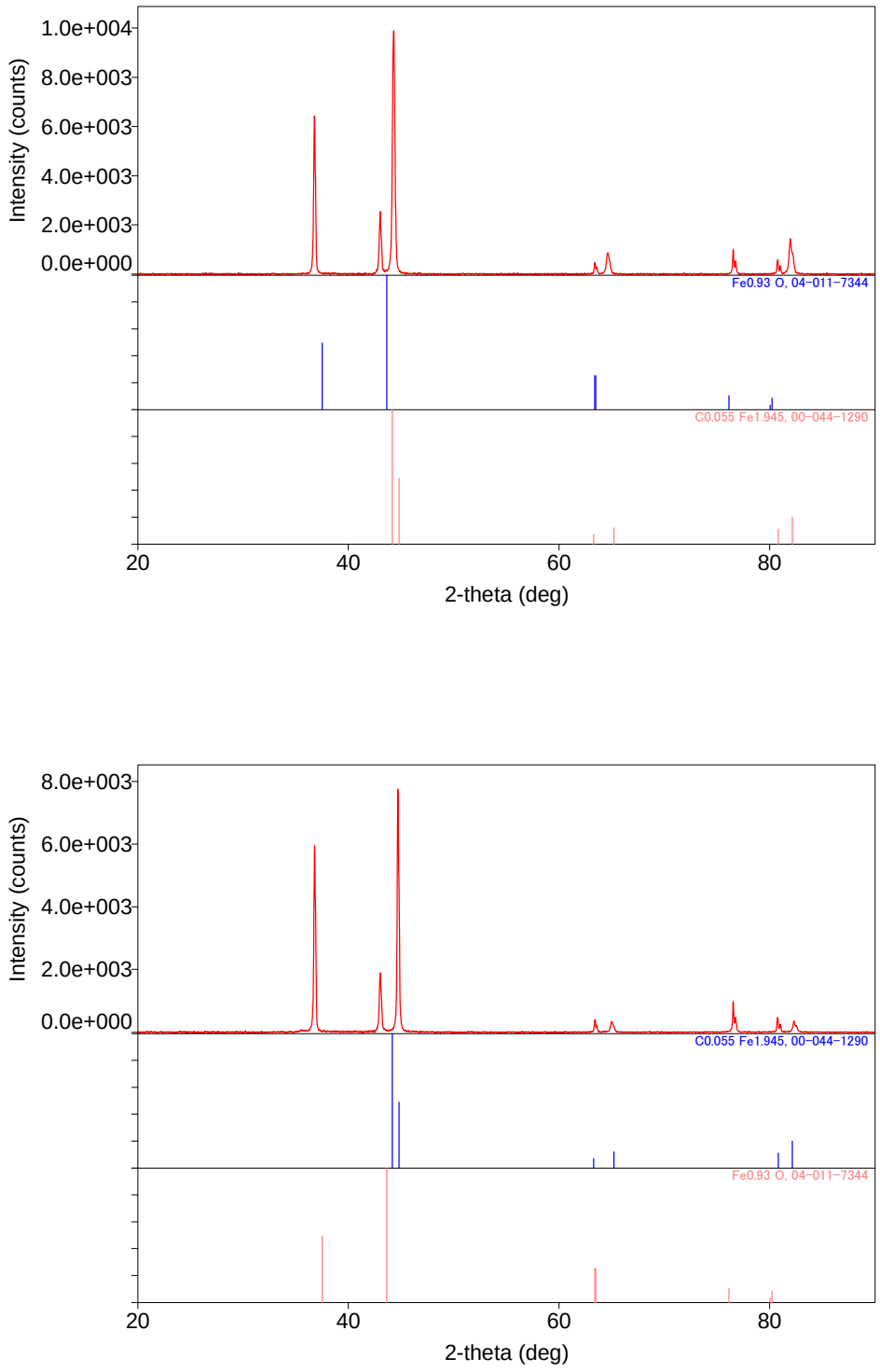

Figure 51. XRD patterns of the iron oxide created after 15 min anodization in 45A/m^2, 25 °C, in a 0.37 wt% NH4F, 0.9 wt% DI water EG solution before (top) and after (bottom) annealing

Summarizing the results of XRD, it is observed that

- Anodization in NaOH solutions is capable of producing magnetite with optimum conditions being the applied voltages of 12.5 V under elevated temperatures of 90 °C. The applied annealing process, however, did not have satisfactory results.
- In EG solutions of 0.50 wt% NH_4F, 3 wt% DI water, the oxide that is finally obtained is hematite under an applied voltage of 50 V at a temperature of 50 °C.
- In EG solutions of 0.37 wt% NH_4F, 1.8 wt% DI water, the finally obtained oxides are wustite ($Fe_{0.93}O$) with magnetite as a secondary phase.
- However, in the galvanostatic anodization, only $Fe_{0.93}O$ oxide is present.

E. CHARACTERIZATION WITH FIB

Based on the observed morphology of HY-80 steel samples anodized in various conditions, highly ordered iron oxide nanopores are formed during galvanostatic anodization in EG solutions containing 0.37 wt% NH_4F and 0.9 wt% DI water. FIB milling was carried out on samples that have been anodized under these conditions to observe the cross sectional features of the oxide film. Specifically the oxide layer growth on the surface of steel samples anodized under constant current density of 45 A/m^2 was studied.

The thickness of the oxide layer was measured by using FIB to create a transverse incision on the surface of the specimen, allowing SEM to examine its morphology and take the pictures that appear in Figures 52 and 53. The obtained oxide layer after a 5 min anodization is quite thin, with thickness varying between 490 to 140 nm. However, by increasing the anodization time, thickness also increases, and in a 15 min anodization, a layer of 290 to 650 nm thickness was observed.

The width of the walls of columns around pores was also calculated. In the 5 min anodization, the column surrounding each pore had an average width of 55 nm, but as the layer grew, so did the width of the walls, and after 15 min of anodizing, it reached an average width of 66 nm.

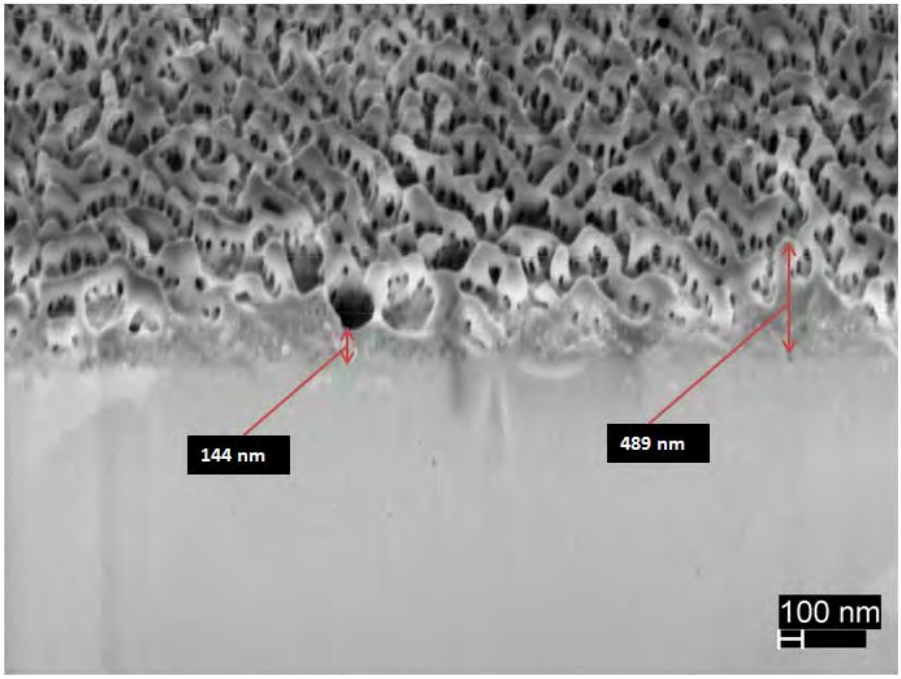

Figure 52. FIB image of anodized steel surface under current density of 40 A/m^2 in EG solution of 0.37 wt% NH_4F, 0.9 wt% DI water concentration, for 5 min

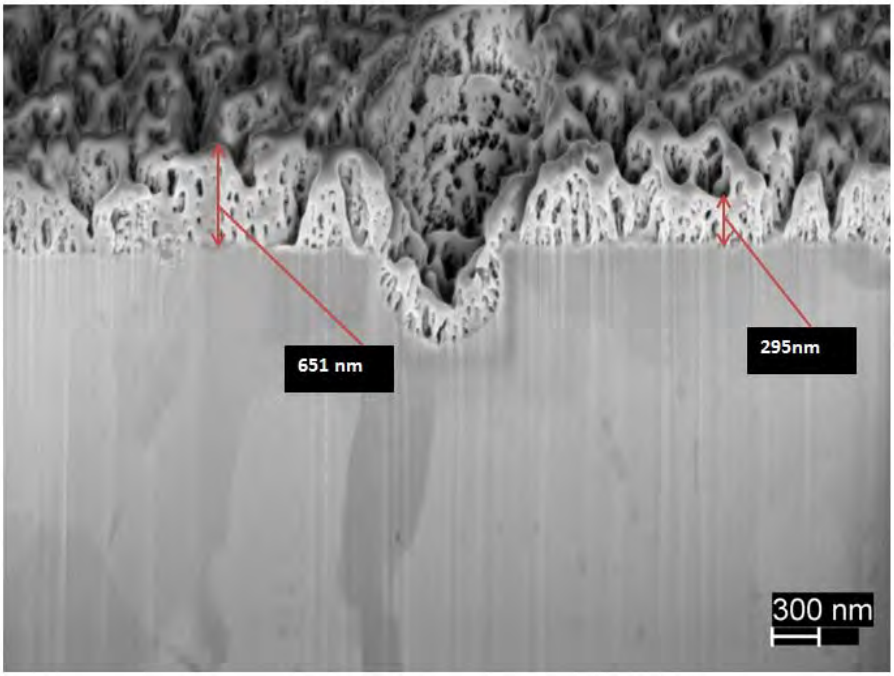

Figure 53. FIB image of anodized steel surface under current density of 45 A/m^2 in EG solution of 0.37 wt% NH_4F, 0.9 wt% DI water concentration, for 15 min

Another interesting observation made from FIB examination, is that the nanoporous structure expands in the whole area that had been exposed in anodization, covering also the defects of the surface, such as the pit in Figure 53. This is significant since the anodization process is capable of mimicking the surface topography of the underlying metallic surface quite well and thus will not provide sites of crevice corrosion on the surface.

FIB analysis showed that by galvanostatic anodization, a nanoporous structure can be manufactured on the surface of steel whose depth can be adjusted through anodization time beginning from 490 nm corresponding to a 5 min anodization. Moreover, by increasing anodization time, the wall thickness around pores increases as well. Clearly, future experiments can focus on optimizing the anodization process to produce the required thickness of protective oxide film.

F. CONTACT ANGLES

Initially, a large number of tests were conducted in order to evaluate the hydrophobicity of the steel surfaces by determining the average contact angle of DI water droplets on the polished surface of HY-80 steel. After the completion of 33 experiments, an average angle of 71° was measured with a standard deviation of 9.4°, as seen in the histogram in Figure 54. These tests proved the hydrophilic character of HY-80.

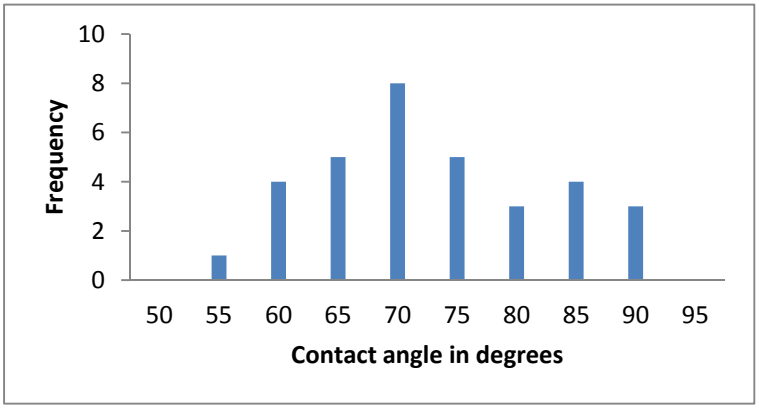

Figure 54. Histogram of contact angles for plain steel

The anodized surface showed a change in its wettability properties from slightly hydrophilic to hydrophobic behavior. In each anodization method applied, the behavior of the steel remained hydrophobic. Photographs in Figure 55 show a comparison of the appearance of the water drops on various surfaces as indicated. The measured data are summarized in Tables 11 and 12. The best results, however, were obtained using anodization in a NaOH solution. The anodized samples showed contact angles varying in a range of 131° to 146°. The largest contact angles were reported when applying a voltage of 12.5 V in an electrolytic temperature of 90 °C for a period of time between 3 min (146°) and 10 min (145°).

When EG-based electrolyte was used, the produced surfaces were slightly less hydrophobic, with contact angles varying between 110° and 138°. The surfaces manufactured with this method decreased in wettability as the concentration of NH_4F in the solution increased. Therefore, the greatest contact angles were observed when anodizations took place in 0.50 wt% NH_4F solutions, and particularly under voltage of 50 V, at 60 °C for a duration of 5 min, a contact angle of 138° appeared, which was the maximum obtained for this solution. The surfaces created in 0.37 wt% NH_4F electrolyte appear to have similar wetting properties. In the case of potentiostatic anodization in 1.8 wt% DI water concentration, the maximum contact angle was 118° and appeared after anodizing under voltage of 30 V for 1 hour, while in the case of galvanostatic anodization under a constant current density of 82 A/m² at room temperature for 15 min, a 126° angled was achieved.

Table 11. Contact angles of DI water on the surface of anodized steel under NaOH electrolyte

Anodization condition	7.5 V	12.5 V
75 °C – 5 min	134°	136°
90 °C – 3 min		146°
90 °C – 5 min	131°	
90 °C – 10 min		145°

Table 12. Contact angles of DI water on the surface of anodized steel under various EG-based electrolytes

	Anodiz. condition	30 A/m²	45 A/m²	60 A/m²	85 A/m²	10 V	20 V	25 V	30 V	40 V	50 V
0.50 wt% NH_4F, 3 wt% DI water	50 °C								121°	123°	
	60 °C					121°		123°	111°	120°	138°
0.37 wt% NH_4F, 1.8 wt% DI water							117°		118°		112°
0.37 wt% NH_4F, 0.9 wt% DI water	5 min	121°	118°		113°						
	15 min		124°	110°	126°						

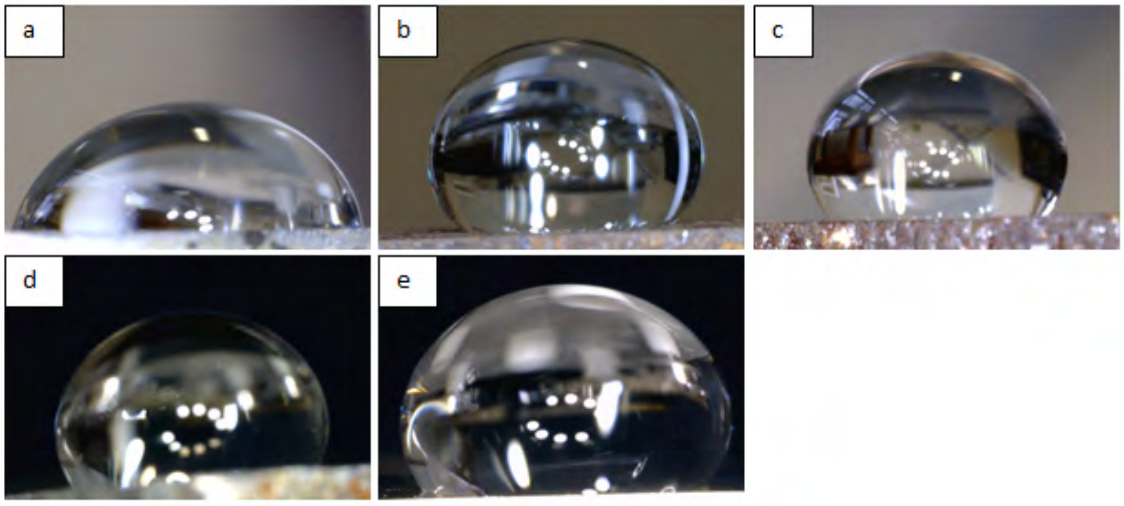

Figure 55. Pictures of contact angles (a) on the surface of polished steel, and on the surfaced of anodized steels under (b) NaOH electrolyte in 7.5 V, 75 °C for 5 min, (c) 0.50 wt% NH_4F, 3 wt% DI water, EG electrolyte in 50 V, 60 °C for 5 min, (d) 0.37 wt% NH_4F, 1.8 wt% DI water, EG electrolyte in 30 V, room temperature for 1 hour, and (e) 0.37 wt% NH_4F, 0.9 wt% DI water, EG electrolyte in 45.2 A/m², room temperature for 5 min

G. CORROSION RESISTANCE

For each anodization technique presented in this paper, selected samples were examined for their corrosion resistance. Following the procedure described in Chapter III, the weight loss corrosion rates determined are shown in Table 13.

Table 13. Corrosion rates for HY-80

	Mass loss (mg/mm^2)	MPY	mm/yr
corrosion in seawater			
polished steel	0.030	4.955	0.1258
anodized in NaOH solution	0.031	5.083	0.1291
anodized in 0.50 wt% NH_4F, 3 wt% DI water, EG solution	0.044	7.387	0.1876
anodized in 0.37 wt% NH_4F, 1.8 wt% DI water, EG solution	0.028	4.600	0.1168
anodized in 0.37 wt% NH_4F, 0.9 wt% DI water, EG solution	0.029	4.759	0.1209
corrosion in salt water			
polished steel	0.032	5.355	0.1360
anodized in NaOH solution	0.051	8.518	0.2164
anodized in 0.50 wt% NH_4F, 3 wt% DI water, EG solution	0.078	12.967	0.3294

As can be deduced from Table 13, the corrosion in seawater was less than the corrosion experienced in 3.5wt % NaCl solution. Moreover, not all of the anodized surfaces displayed improved anticorrosive properties. Especially anodization under 0.50 wt% NH_4F, 3 wt% DI water, the EG solution worsened the corrosive properties of the steel by far, while in the case of anodization under a NaOH solution, the corrosion rates increased but at a lesser grade.

However, the self-oriented nanoporous structures created on anodized samples under EG-based solutions of 0.37 wt% NH_4F concentration granted HY-80 steel corrosion protection. Specifically, the corrosion rate of steel dropped from 5 MPY to a range between 4.6 to 4.8 MPY.

H. BIOFOULING

1. Thermal Analysis

Preliminary thermal analysis was conducted on selected HY-80 specimens in order to verify the capability of these techniques to detect organic material depositions on the surface of steel. During those examinations, the main focus was the identification of carbon traces, which are indicative of the presence of living organisms such as bacteria and micro-organisms. For this reason, four different samples were prepared in the following conditions:

1. polished steel
2. polished steel with the addition of mold
3. polished steel left to corrode inside stagnant natural water for one week
4. polished steel left to corrode inside 3.5 wt% NaCl solution for one week

Each of these samples was analyzed with TGA, DSC, and QMS techniques; the aggregate results can be seen in Figures 56, 57, and 58.

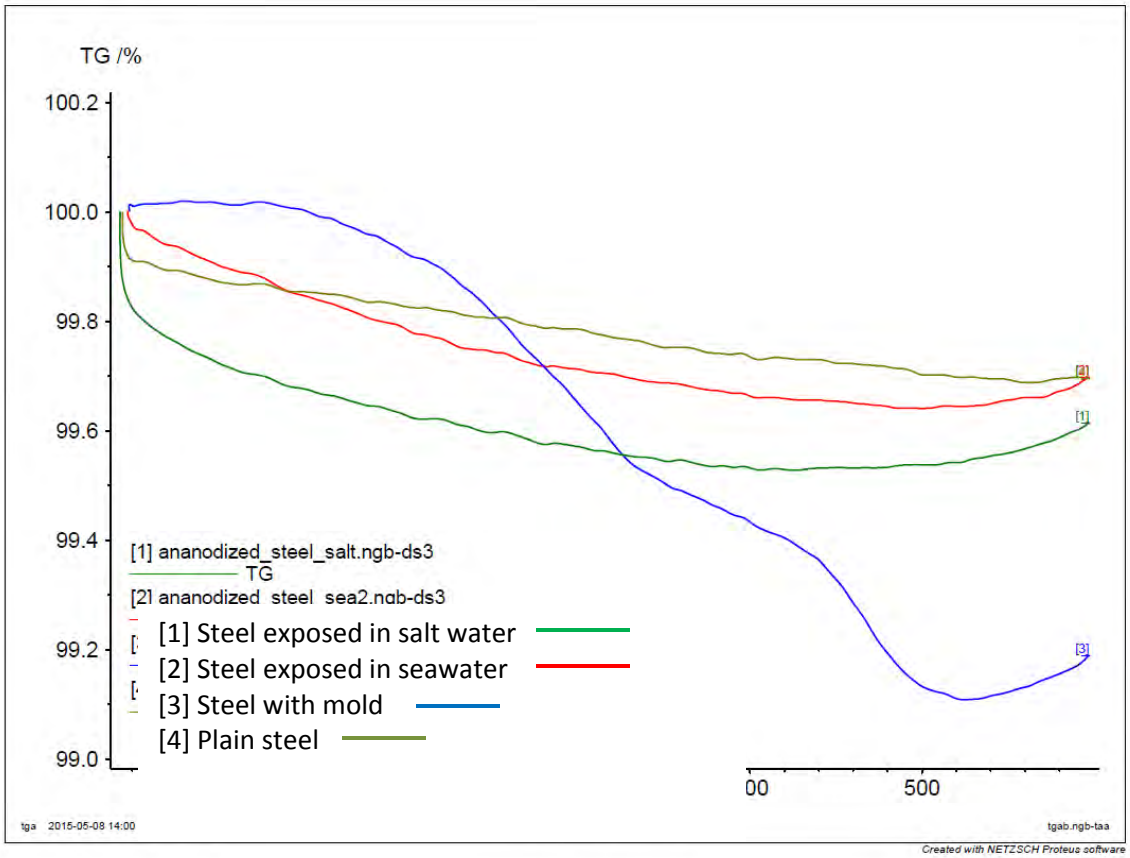

Figure 56. TGA analysis

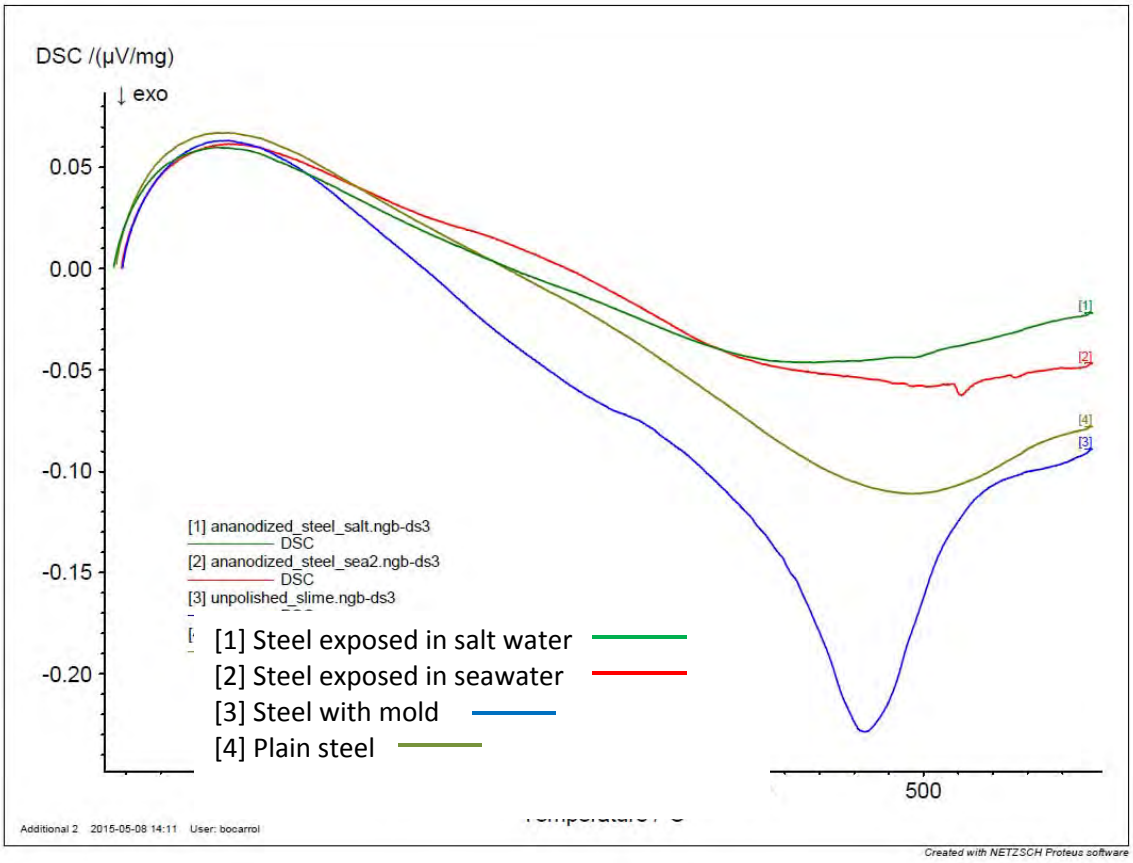

Figure 57. DSC analysis

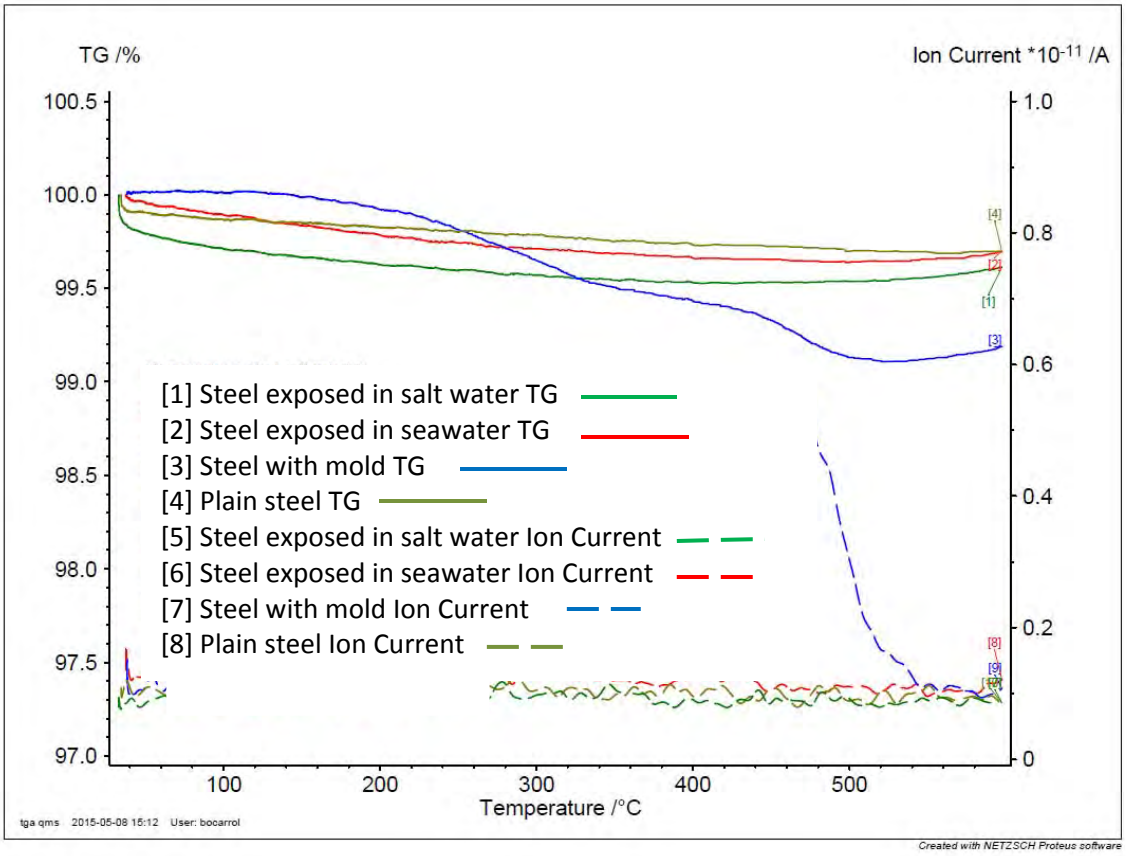

Note. The noticeable red dotted line shows the emission of CO_2 gases at 470 °C on the steel specimen with the mold.

Figure 58. TGA/QMS diagram

As expected, the DSC curve of the sample with mold presented a distinguish slope as a result of an exothermic reaction at 470 °C, which was later examined through QMS and found to be carbon combustion and the creation of CO_2 gases. Moreover, both the untreated steel and that corroded in 3.5wt% NaCl-DI water solution samples exhibited similar curves that did not display any slope due to carbon combustion and, furthermore, no emission of CO_2 gases was recorded. In the test involving the steel sample that was exposed in seawater, again no traces of carbon were found. The last experiment was then repeated with another HY-80 steel sample corroded under the same conditions as the previous, trying to verify the results, but again the analysis produced similar data.

Therefore, the conclusion can be made that either there was no micro-organism attachment onto the surface of the sea-corroded samples, or the thermal methods could not identify it, presumably due to the extremely low concentrations of bio organisms present in the small quantity of seawater used in these experiments. The fact that the behavior in the natural seawater (which may have some organic species present in it) was identical to that of the 3.5wt% NaCl -DI water solution, which most likely did not have any biofilm-producing matter in it, supports this speculation. Anyway, the use of the thermal method analysis to assess the content of biofouling on the surface requires an examination with more controlled experiments with controlled amounts of microorganisms introduced in the corrosive solutions; other characterization methods should also be investigated.

2. SEM/EDS Analysis

Following the inconclusive nature of the TGA studies, SEM and EDS examinations were performed in order to verify the existence of living microorganisms on the surface of steel left in seawater over a period of 10 days. In order to compare the features formed on the steel surface exposed to marine conditions, both natural Monterey seawater and a 3.5wt%NaCl in DI water solution were examined since the latter solution does not contain any significant amount of microorganisms present in it. Figure 59 shows a secondary electron image showing the typical appearance of the corrosion product formed in the DI water–3.5wt%NaCl solution, and the EDS analysis confirmed the presence of mostly Fe and O.

SEM images of steel plates that had been left in natural seawater revealed not only the usual characteristic presence of iron oxides and rust, but also several distinct features with dimensions varying from 9 μm to 81 μm, as depicted in Figures 60 and 61. This observation has led to the deduction that the appearance of these features is something exclusively associated with the contents of ocean water.

EDS analysis on these morphologies revealed the elemental composition of these crystals to be rich in carbon as well as calcium, magnesium, and oxygen, as seen in Figure 63 and Table 16. However, the EDS analysis for oxygen that is shown is not accurate due to the high errors associated with low atomic number elements in this technique. In spite of the increased content of organic compounds, the observed shapes do not correspond to living microorganisms, but have been identified as calcium carbonate ($CaCO_3$) crystals, which are known to grow on steel surfaces. The presence of Ca^{2+} and Mg^{2+} in seawater creates a cathodic reduction of oxygen under the following equations which precipitate in $CaCO_3$ and $Mg(OH)_2$ [46]:

$$Ca^{2+} + HCO_3^- + OH^- \rightarrow H_2O + CaCO_3 \quad (9)$$

$$Mg^{2+} + 2OH^- \rightarrow Mg(OH)_2 \quad (10)$$

The resulting $CaCO_3$ crystals can appear in many crystalline forms, as illustrated in Figure 64. The optical resemblance with the obtained carbon-enhanced shapes on the surface of HY-80 plates is obvious; therefore, they are identified as calcites and aragonites (crystalline forms of calcium carbonate). Extensive SEM/EDS examination did not show any traces of bacteria or other microorganisms. This could be due to the low content of microorganisms in the ocean water used in the experiments, thus further investigation should be done with microbiological techniques such as bacteria cultivation and colonization. These microscopy results are in agreement with the TGA results that showed no measurable carbon decomposition during thermal exposure of the seawater-corroded samples.

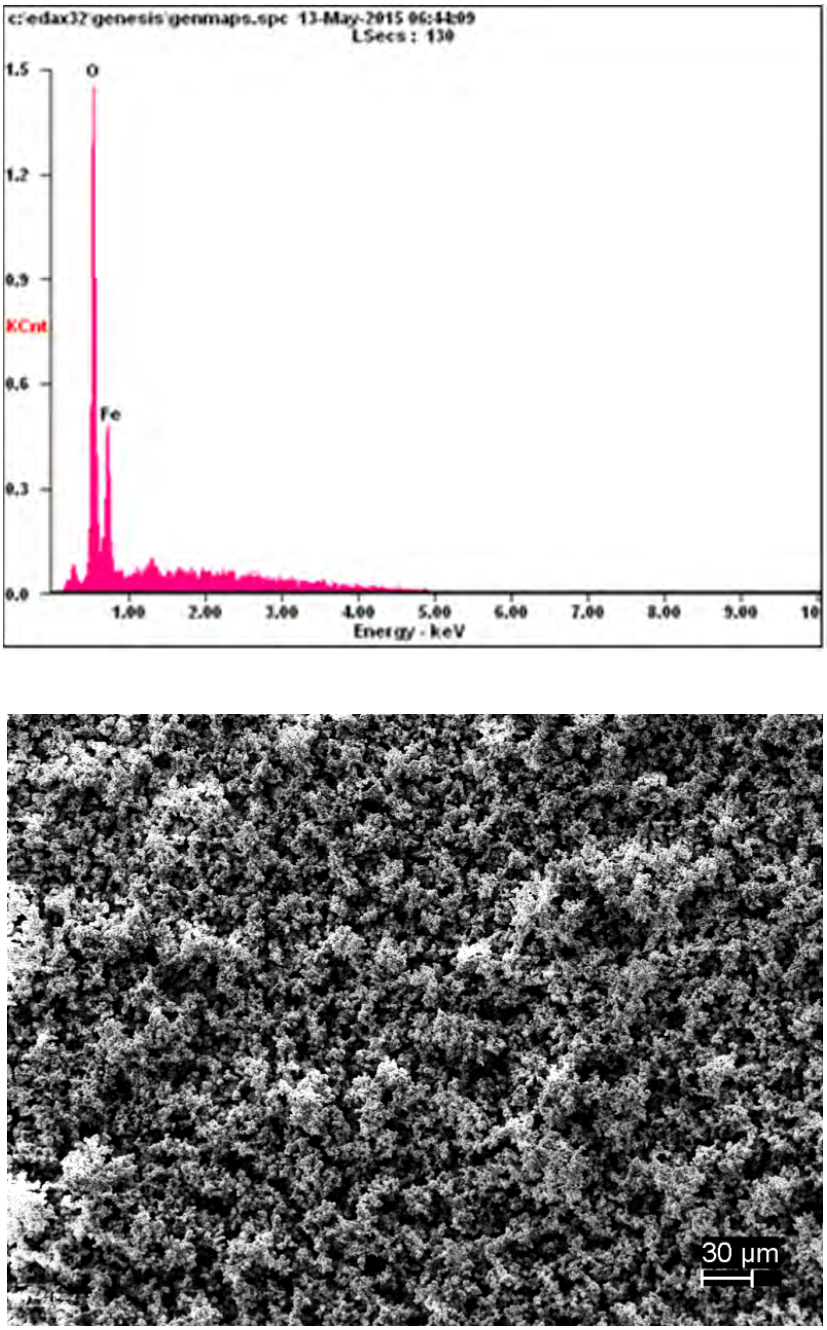

Figure 59. EDS spectrum from the iron oxide formed on the surface of polished steel plate left in DI water–3.5wt% NaCl solution for 10 days

Table 14. EDS quantitative analysis showing weight and atomic number percent of elements of iron oxide appearing in Figure 59

Element	Wt%	At%
Oxygen (O)	29.78	59.69
Iron (Fe)	70.22	40.31
Matrix	Correction	ZAF

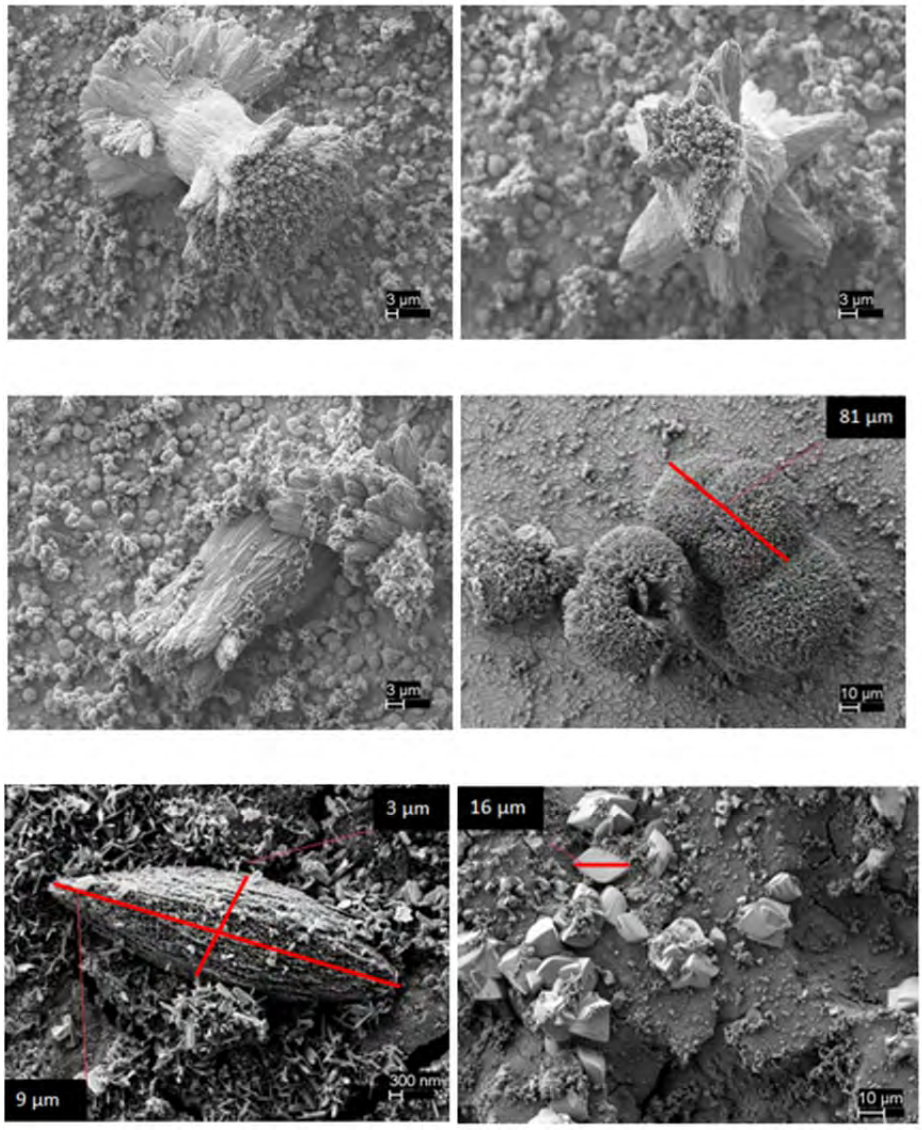

Figure 60. SEM images of calcium carbonate ($CaCO_3$) crystals with their corresponding dimensions appearing in red lines

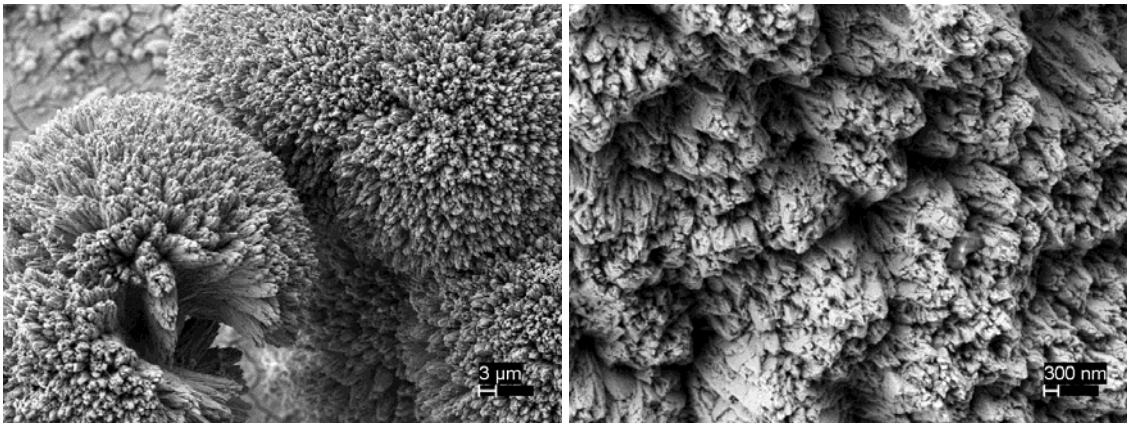

Figure 61. SEM images of aragonite crystal in low (left) and high (right) magnification

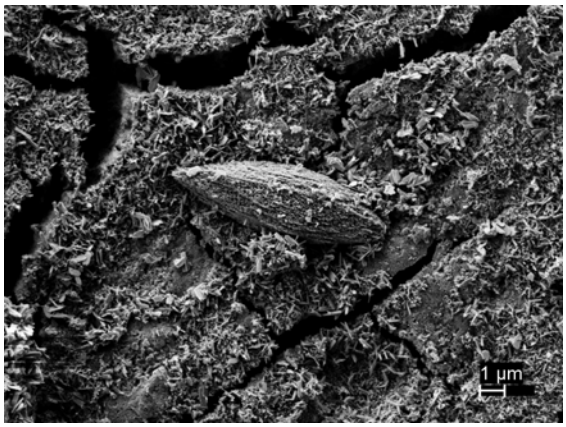

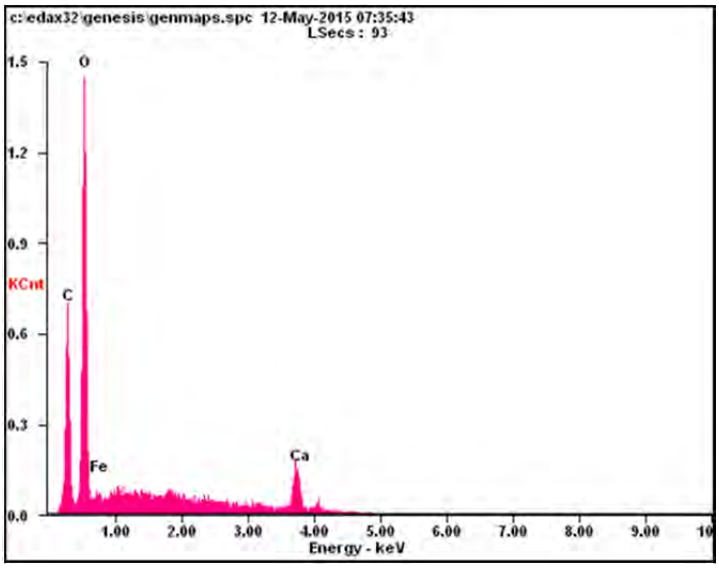

Figure 62. EDS spectrum from a calcium carbonate ($CaCO_3$) crystal

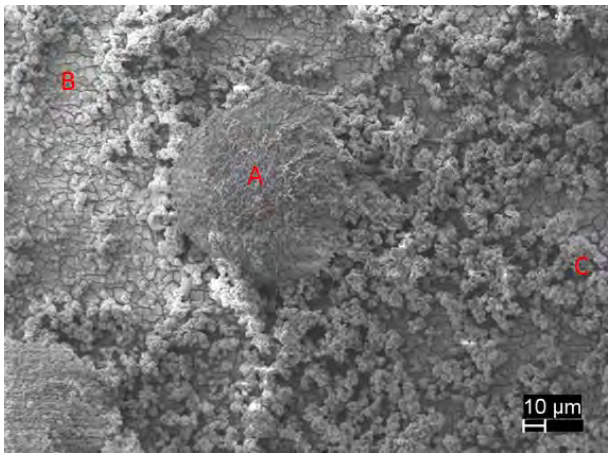

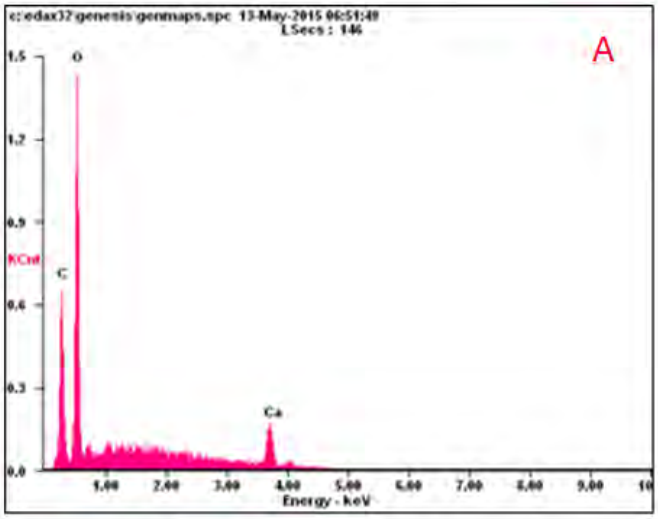

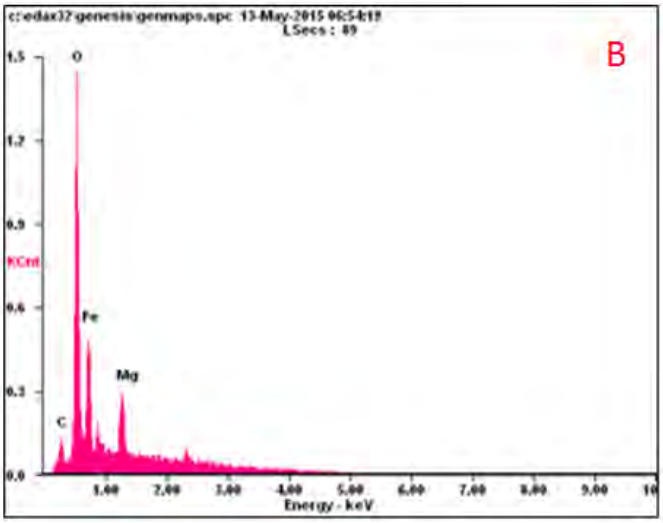

Figure 63, continued on next page

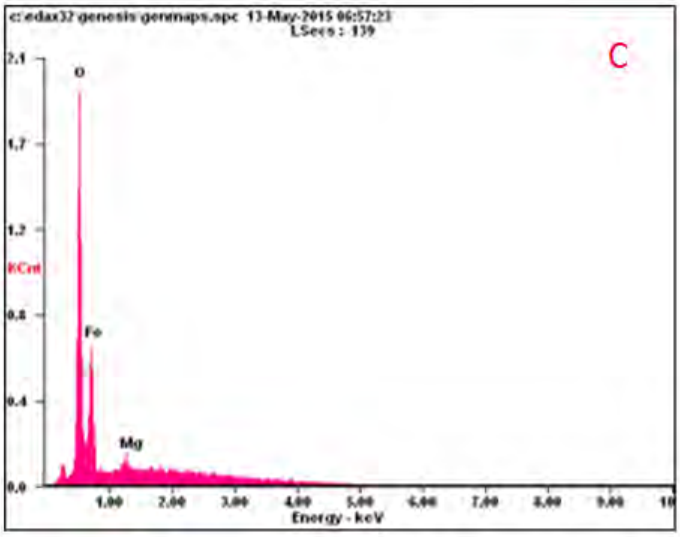

Figure 63. EDS spectrum from corroded steel plate in seawater

Table 15. EDS quantitative analysis showing weight and atomic number percent of elements of the $CaCO_3$ crystal in Figure 62

Element	**Wt%**	**At%**
Carbon(C)	25.44	36.25
Oxygen (O)	53.60	57.33
Iron (Fe)	20.96	6.42
Matrix	Correction	ZAF

Table 16. EDS quantitative analysis showing weight and atomic number percent of elements appearing in the corroded steel surface of Figure 63

Area A		
Element	**Wt%**	**At%**
Carbon (C)	30.12	36.47
Oxygen (O)	69.88	63.53
Matrix	Correction	ZAF

Area B		
Element	**Wt%**	**At%**
Carbon (C)	03.00	07.27
Oxygen (O)	27.18	49.41
Iron (Fe)	59.53	31.01
Magnesium (Mg)	10.29	12.32
Matrix	Correction	ZAF

Area C		
Element	**Wt%**	**At%**
Oxygen (O)	28.65	57.54
Iron (Fe)	69.48	39.98
Magnesium (Mg)	01.87	02.48
Matrix	Correction	ZAF

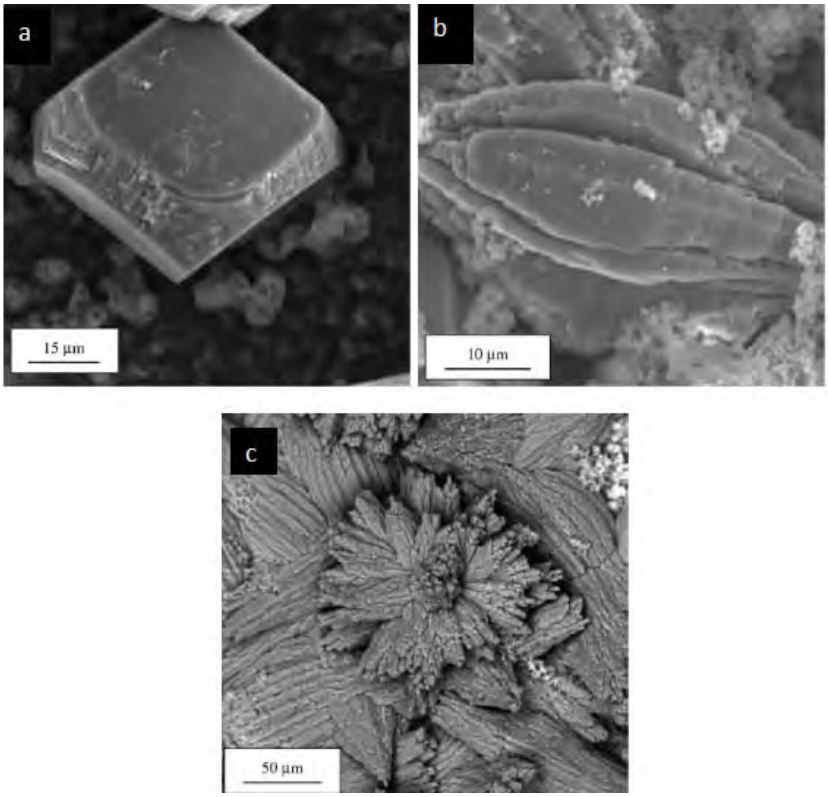

Figure 64. SEM images of various crystalline forms of $CaCO_3$ crystals such as calcite in (a) and aragonite in (b) and (c), from [46]

THIS PAGE INTENTIONALLY LEFT BLANK

VI. CONCLUSIONS

This study shows that homogenous nanoporous anodic films can be formed on HY-80 steels in an EG solution containing ammonium fluoride and water electrolyte. However, the increased concentration of water in combination with elevated temperatures resulted in the severe pitting of the surface of the anodized specimen and in the creation of nano channeling patterns that affected the uniformity of the surface oxide layer. Nevertheless, by decreasing anodization temperature and water concentration, homogenous nanoporous oxide layers were successfully produced by the following two methods.

Through potentiostatic anodization in a range between 20 to 30 V in a 0.37 wt% NH_4F, 1.8 wt% DI water EG solution at room temperature, homogenous nanoporous anodic films were produced. However, the optimum anodization conditions are under 30 V for 1 hour with a solution maintained at approximately 25 °C, which creates an oxide layer with a 120 nm average pore diameter. Furthermore, by annealing the sample at 400 °C for 2 hours, it transforms into wustite ($Fe_{0.93}O$) and magnetite. The produced surface exhibits decreased wettability, with a water contact angle of approximately 118°, which is an improvement in the wetting properties of polished HY-80 by 166%. It also reduced the corrosion rate of HY-80 steel by approximately 7.2%.

The second successful technique of constructing a highly oriented nanoporous oxide is through galvanostatic anodization in a current density range between 30 and 85 A/m^2 in 0.37 wt% NH_4F, 0.9 wt% DI water EG solution at room temperature. In this method, the optimum anodizing condition is under 45 A/m^2 on an approximately 25 °C solution for 15 min. This results in the formation of a 290 nm to 650 nm thick oxide with an average 66 nm distance between each pore. The crystal structure of the oxide is that of wustite ($Fe_{0.93}O$) and through the annealing process, its structure remained unaffected. Again, in this case, the surface oxide topography granted the steel exceptional hydrophobic behavior

(124°) with water contact angles 177% greater than those of the untreated HY-80 steel and slightly improved (by 4%) its corrosion properties.

Concluding this study, antifouling properties of the constructed morphologies were examined with the use of both thermal (TGA/DSC) and SEM/EDS quantitative analysis. However, they did not show microorganism attachments during exposure on stagnant natural water, thus antifouling properties need to be examined through experiments with controlled amounts of microorganisms introduced in the corrosive solutions and other characterization methods.

VII. FUTURE WORK

The findings of this study look promising for the use of anodization as a method to impart hydrophobic, anticorrosive, and antifouling properties on naval structural steel. However, they are initial indications and there is a long way before this technique could be successfully used in the shipbuilding and naval engineering industry.

During this research, no examination of the physical and mechanical properties of the as-treated HY-80 steel was made, and it is highly unlikely that the anodized steel maintained its original properties. Therefore, subsequent studies should focus on the analysis of the newly obtained mechanical behavior of the HY-80 steel.

Antifouling evaluation was contacted in a very preliminary stage. Additional microbiological tests should be made through bacteria cultivation and examination of their attachment and colonization process on the anodized surfaces.

Finally, steel is known to be an alloy that is very difficult to anodize. There are other metals such as aluminum- and titanium-based alloys that are more susceptible to anodization and more resistant to corrosion compared to low carbon steel. The duplications of the same nanotopographic structures on their surfaces will provide extra benefits for the marine industry.

THIS PAGE INTENTIONALLY LEFT BLANK

LIST OF REFERENCES

[1] M. P. Schultz et al., “Economic impact of biofouling on a naval surface ship,” *Biofouling*, vol. 27, no.1, 2011.

[2] S. Cao et al., “Progress of marine biofouling and antifouling technologies,” *Chin. Sci. Bulletin*, vol. 56, no. 7, pp. 598–612, Mar. 2011.

[3] Woods Hole Oceanographic Institution (WHOI), “Marine fouling and its prevention,” U.S. Naval Inst., Annapolis, MD, 1952.

[4] J. Chen et al., “Antifouling activity of simple synthetic diterpenoids against larvae of the barnacle Balanus albicostatus Pilsbry,” *Molecules*, vol. 15, no. 11, pp. 8072–8081, 2010.

[5] D. V. Ellis, “New dangerous chemicals in the environment: Lessons from TBT,” *Mar. Pollut. Bull*., vol. 22, no. 1,pp. 8–10, 1991.

[6] R. Vasudevan et al., “Microscale patterned surfaces reduce bacterial fouling-microscopic and theoretical analysis,” *Colloids and Surfaces B: Biointerfaces*, vol. 117, pp. 225–232, May 1, 2014.

[7] M. L. Carman et al., “Engineered antifouling microtopographies—Correlating wettability with cell attachment,” *Biofouling*, vol. 22, no. 1, pp. 11–21, 2006.

[8] B. Bhushan, “Biomimetics inspired surfaces for drag reduction and oleophobicity/philicity,” *Beilstein J. of Nanotechnology*, vol. 2, no. 1, pp. 66–84, 2011.

[9] J. G. Buijnsters et al., “Surface wettability of macroporous anodized aluminum oxide,” *ACS Appl. Mater. Interfaces*, vol. 5, no. 8, pp. 3224–3233, Apr. 24, 2013.

[10] P. V. Mahalakshmi et al., “Enhancing corrosion and biofouling resistance through superhydrophobic surface modification,” *Current Sci.* (Bangalore), vol. 101, no. 10, pp. 1328–1336, Nov. 25, 2011.

[11] J. Ferré-Borrull et al., “Nanostructural engineering of nanoporous anodic alumina for biosensing applications,” *Materials*, vol. 7, no. 7, pp. 5225–5253, 2014.

[12] C. Yao and T. J. Webster, “Anodization: A promising nano-modification technique of titanium implants for orthopedic applications,” *J. Nanosci. and Nanotechnol.*, vol. 6, no. 9–10, pp. 2682–2692, 2006.

[13] M. Dahlström et al., “Surface wettability as a determinant in the settlement of the barnacle Balanus Improvisus (DARWIN),” *J. Exp. Mar. Biol. Ecol.*, vol. 305, no. 2, pp. 223–232, July 16, 2004.

[14] C. Y. Lee et al., “The study of wettability by nitrogen ion beam treatment into aluminum surface,” 2011.

[15] D. Gong et al., “Titanium oxide nanotube arrays prepared by anodic oxidation,” *J. Mater. Res.*, vol. 16, no. 12, pp. 3331–3334, 2001.

[16] J. M. Macak et al., “High-aspect-ratio TiO2 nanotubes by anodization of titanium,” *Angewandte Chemie Int. Edition*, vol. 44, no. 14, pp. 2100–2102, 2005.

[17] W. Wei et al., “High aspect ratio ordered nanoporous Ta 2 O 5 films by anodization of Ta,” *Electrochem. Commun*., vol. 10, no. 3, pp. 428–432, 2008.

[18] J. Zhao et al., “In situ synthesis of zirconia nanotube crystallines by direct anodization,” *Corros. Sci.*, vol. 50, no. 6, pp. 1593–1597, 2008.

[19] W. Lee et al., “Self-ordering behavior of nanoporous anodic aluminum oxide (AAO) in malonic acid anodization,” *Nanotechnol.*, vol. 18, no. 47, pp. 475713, 2007.

[20] G. D. Sulka and W. J. Stępniowski, “Structural features of self-organized nanopore arrays formed by anodization of aluminum in oxalic acid at relatively high temperatures,” *Electrochim. Acta*, vol. 54, no. 14, pp. 3683–3691, 2009.

[21] G. Sulka et al., “Synthesis of well-ordered nanopores by anodizing aluminum foils in sulfuric acid,” *J. Electrochem. Soc*., vol. 149, no. 7, pp. D97–D103, 2002.

[22] T. Burleigh et al., “Anodizing steel in KOH and NaOH solutions,” *J. Electrochem. Soc.*, vol. 154, no. 10, pp. C579–C586, 2007.

[23] T. Burleigh et al., “Properties of the nanoporous anodic oxide electrochemically grown on steel in hot 50% NaOH,” *J. Electrochem. Soc.*, vol. 156, no. 1, pp. C45–C53, 2009.

[24] T. D. Burleigh, “Method of anodizing steel,” U.S. Patent 20110284390 A1, Nov. 24, 2011.

[25] K. Xie et al., “Fabrication of iron oxide nanotube arrays by electrochemical anodization,” *Corros. Sci*., vol. 88, pp. 66–75, Nov. 2014.

[26] S. P. Albu et al., “High aspect ratio, self-ordered iron oxide nanopores formed by anodization of Fe in ethylene glycol/NH4F electrolytes,” *Physica Status Solidi (RRL)-Rapid Res. Lett.*, vol. 3, no. 2–3, pp. 64–66, 2009.

[27] Y. Konno et al., “Formation of self-organized nanoporous anodic films on carbon steel,” *ECS Trans*., vol. 50, no. 37, pp. 183–190, 2013.

[28] W. Zhan et al., “Formation of nanopore arrays on stainless steel surface by anodization for visible-light photocatalytic degradation of organic pollutants,” *J. Mater. Res*., vol. 27, no. 18, pp. 2417–2424, Sept. 28, 2012.

[29] M. E. Callow and J. A. Callow, “Marine biofouling: A sticky problem,” *Biologist*, vol. 49, no. 1, pp. 1–5, 2002.

[30] L. D. Chambers et al., “Modern approaches to marine antifouling coatings,” *Surface and Coatings Technol.*, vol. 201, no. 6, pp. 3642–3652, Dec. 4, 2006.

[31] S. R. Heller et al., “An evaluation of HY 80 steel as a structural material for submarines,” *Nav. Eng. J*., vol. 77, no. 1, pp. 29–44, 1965.

[32] E. J. Czyryca and M. G. Vassilaros, “Advances in low carbon, high strength ferrous alloys (research and development report),” Naval Surface Warfare Center, Bethesda, MD, Tech. Rep. AD-A265264, CDNSWC/SME-92/64, Apr. 1993.

[33] J. Ritter and N. Balwin, “Properties of HY-100 steel for naval construction,” Australian Dept. of Defence, Materials Res. Laboratory, Melbourne, Victoria, Tech. Rep. MRL-R-1149, 1989.

[34] Naval sea systems command, Department of Navy. (n.d.). MIL-S-16216, Military specification of steel plate, alloy, structural, high yield strength (HY-80 and HY-100). Online: http://everyspec.com/MIL-SPECS/MIL-SPECS-MIL-S/MIL-S-16216K_11494/

[35] T. Holmquist, “Strength and fracture characteristics of HY-80, HY-100, and HY-130 steels subjected to various strains, strain rates, temperatures, and pressures,” Naval Surface Warfare Center, Dahlgren, VA, Rep. NSWC TR 88–252, 1987.

[36] W. Lin, “Anodized aluminum oxide and its application for organic transistors and sensors,” Ph. D. dissertation, Dept. Elect. Eng., Katholieke Universiteit Leuven, Heverlee, Belgium, July 5, 2012.

[37] L. Yang, Ed., “Materials characterization: Introduction to microscopic and spectroscopic methods,” Ringgold Inc., Portland, OR, 2008.

[38] R. Hausman, “Development of low-biofouling polypropylene feed spacers for reverse osmosis,” Ph. D. dissertation, Dept. Eng., University of Toledo, Toledo, Spain, December, 2011.

[39] J. Melngailis, “Focused ion beam technology and applications,” *J. Vacuum Sci. & Technol. B*, vol. 5, no. 2, pp. 469–495, 1987.

[40] L. A. Giannuzzi and F. A. Stevie, “Introduction to focused ion beams: Instrumentation, theory, techniques and practice,” Springer Science & Business Media, New York, NY, 2005.

[41] S. Reyntjens and R. Puers, “A review of focused ion beam applications in microsystem technology,” *J. Micromech. Microengineering*, vol. 11, no. 4, pp. 287–300, 2001.

[42] C. A. Volkert and A. M. Minor, “Focused ion beam microscopy and micromachining,” *MRS Bull*., vol. 32, no. 5, pp. 389–399, 2007.

[43] M. N. Mowry, “In situ Raman spectroscopy study of the formation of graphene from urea and graphite oxide,” Master’s thesis, Dept. Mech. Eng., Naval Postgraduate School, Monterey, CA, September, 2012.

[44] D. A. Jones, “Principles and prevention of corrosion,” Upper Saddle River, NJ: Prentice Hall, 1996.

[45] N. Mukherjee et al., “Fabrication of nanoporous tungsten oxide by galvanostatic anodization,” *J. Mater. Res.*, vol. 18, no. 10, pp. 2296–2299, 2003.

[46] H. Möller, “The influence of Mg 2 on the formation of calcareous deposits on a freely corroding low carbon steel in seawater,” *Corros. Sci.*, vol. 49, no. 4, pp. 1992–2001, 2007.

INITIAL DISTRIBUTION LIST

1. Defense Technical Information Center
   Ft. Belvoir, Virginia

2. Dudley Knox Library
   Naval Postgraduate School
   Monterey, California